



Numerical studies on small rotor configurations with validation using acoustic wind tunnel data

Jianping Yin¹ · Karl-Stephane Rossignol² · Lukas Rottmann¹ · Thorsten Schwarz¹

Received: 23 January 2023 / Revised: 25 May 2023 / Accepted: 31 May 2023
 © The Author(s) 2023

Abstract

This paper addresses the acoustic and aerodynamic characteristics of small rotor configurations, including the influence of the rotor–rotor interactions. For this purpose, a Rotor/Rotor/Pylon configuration is chosen for both the test and numerical simulations. The wind tunnel experiments on various rotor configuration were performed in DLR’s Acoustic Wind Tunnel Braunschweig (AWB). The experiments involve isolated rotors, and rotors in tandem and coaxial configuration in hover and forward flight. For numerical simulations, an unsteady free wake 3D panel method (UPM) is used to account for aerodynamic non-linear effects associated with the mutual interference among the Rotor/Rotor/Pylon configurations. The effect of the pylon is simulated using potential theory in form of a panelized body. Finally, the sound propagation into the far field is calculated with DLR’s FW–H code APSIM, using UPM blade surface pressure as input. The validation effort is supported by CFD TAU steady simulations on selected hover test cases. The experiments and numerical results indicate that the noise at the blade passing frequency (BPF) and its higher harmonics is the dominant source of the noise for the present rotor selection. The extra subharmonics between two BPFs appearing in the results are caused by the small geometric discrepancy between the blades as well as the motor noise. Broadband noise is also observed in the experiment, but its contribution to the overall sound pressure is very small and can be neglected. The simulation of the acoustic scattering from the rotor support system for the isolated rotor cases indicated an influence about 1–3 dB on the overall sound pressure of the polar microphones. In both the coaxial and the tandem configuration, the acoustic interferences are particularly well visible in the numerical simulations and cause a more complex noise directivity. There is almost no change in time-averaged inflow by applying phase angles. In the coaxial condition, in hover, the phase delay between rotors does not change the maximum noise level. In forward flight, the phase delay can influence the maximum level of the noise radiation. In both coaxial and tandem configuration, the position of the downstream rotor is key for the noise radiation, and therefore, avoiding the interaction with upstream wake can reduce the noise radiation.

Keywords Small rotor aeroacoustics · Rotor–rotor interactions/interferences · Acoustic analogy APSIM · Unsteady Panel Method UPM · Subharmonics · CFD TAU · UAV · UAM

Abbreviations

$C_N M^2$	Normal force coefficient
D	Rotor diameter (0.33 m)
f	Frequency
M_h	Hover tip mach number

p_0	Air pressure in undisturbed medium, pa
rev	Revolution
T	Thrust in N
V_∞	Flight speed, m/s
Φ	Azimuth angle, deg
θ	Polar angle, deg
$\Delta\delta$	Correction on blade pitch angle
APSIM	DLR FW–H code
AWB	Acoustic wind tunnel in braunschweig
BEM	Boundary element method
BPF	Blade Passing Frequency, Hz
FW–H	Ffowcs-Williams/Hawkings acoustic analogy
LHR	Left-handed rotor
OASPL	Overall sound pressure level, dB

✉ Jianping Yin
jianping.yin@dlr.de

¹ Institute of Aerodynamics and Flow Technology, Helicopter, German Aerospace Center (DLR), Lilienthalplatz 7, 38108 Braunschweig, Germany

² Institute of Aerodynamics and Flow Technology, Acoustic, German Aerospace Center (DLR), Lilienthalplatz 7, 38108 Braunschweig, Germany

RHR	Right-handed rotor
RPM	Rotor rotations per minute
SPL	Sound pressure level, dB
TAU	DLR unstructured computational fluid dynamics code
UPM	Unsteady panel method

1 Introduction

In the context of a growing interest in developing Urban Air Mobility (UAM) solutions to congestion problems in urban traffic, there is a need to provide answers to fundamental questions about the aerodynamic and acoustic properties of these new vehicles [1, 2]. Urban Air Mobility Vehicles (UAMVs) usually refer to small aircraft capable of transporting one to five passengers for intercity transportation. Currently, many different vehicle designs have been proposed and investigated. Examples of concepts related to these new configurations include the eVOLO from Volocopter with 18 single propellers, the CityAirbus from Airbus Helicopter equipped with 4 ducted counter rotating propellers or Joby Aviation's S4 with six tilting single propellers. A number of eVTOL vehicle concepts with different layouts are presented by Johnson et al. [3, 4]. Usually open rotors are selected which are significant sources of tonal and broadband noise. The study by Tinney and Valdez [5] demonstrated that when aircraft have two or more main rotors, rotor–rotor interaction can have significant impact on, among others, performance, and noise. To be publicly accepted, the noise of Urban Air Vehicles must be barely audible compared to the city's background noise. Therefore, Urban Air Vehicles must be designed from the beginning to meet stringent noise standards. The design of low-noise multirotor rotorcraft requires an in depth understanding of the physics related to noise sources. The main noise sources for conventional helicopters are well known, for example the blade–vortex interaction noise (BVI) in the descent flight, but using distributed single or coaxial rotors or ducted rotor, the multiple interactions among rotors, rotor–airframe and the rotor–wake interactions may play an important role in the total noise signal. For example, the study of the small rotor–airframe interaction noise by Zawodny and Boyd [6] indicated that close proximity of airframe surfaces results in the generation of considerable tonal acoustic content in the form of harmonics of the rotor blade passage frequency. The study in [7–9] showed that the broadband noise components have a greater importance in the overall sound emission as blade tip Mach numbers are relatively low, and thus, tonal source components are expected to be dominant only for the first few harmonics. In addition, testing in [7, 8] demonstrated the significant impact of

closely spaced rotor and airframe components on tonal noise generated by the vehicle.

In general, still many noise issues related to the multirotor, such as interactions with complicated inflow, the scattering of airframe, and acoustic interference, still need to be clarified and a basic understanding of the multirotor noise source characteristics still needs to be established. Therefore, this paper will focus on the results from numerical activities for the simple small rotor configurations, especially rotor/rotor configurations and their comparisons with selected wind tunnel test data. For this purpose, the experimental approach used to obtain data will be first presented. The methodologies applied in the numerical simulations will then be described. The acoustic predictions for various rotor configurations will be analyzed and validated with available experimental and CFD results. The analysis also includes the different sources of noise in the test data. The acoustic results will be presented in terms of the overall sound pressure-level (OASPL) directivities and the spectrum.

2 Description of wind tunnel model and test

Validation cases for the prediction of noise emissions of the small rotors are taken from DLR AACID (Acoustics and Aerodynamics for City Drones) wind tunnel tests carried out in 2021. Completed AWB (Acoustic Wind Tunnel Braunschweig) measurement for several propeller configurations include isolated, coaxial, tandem with vertical and lateral offset, as shown in Figs. 1, 2 and 3.

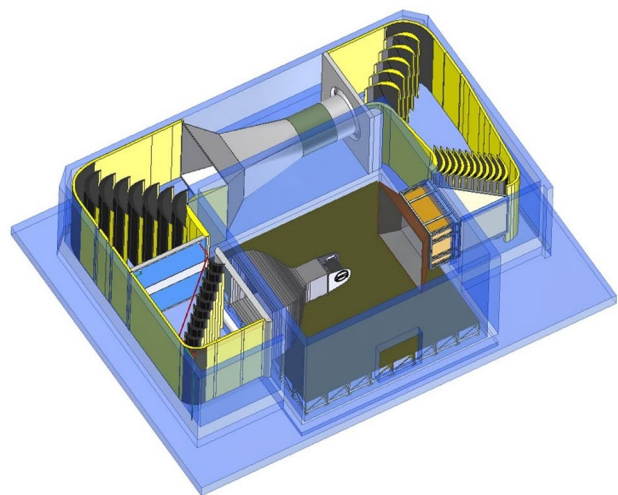


Fig. 1 The Acoustic Wind tunnel Braunschweig (AWB)

Fig. 2 Experimental setup: single rotor (left), coaxial rotors (middle) and tandem rotors (right)



2.1 Test setup

The AWB [10] (e.g., Fig. 1) is DLR's small-scale high-quality anechoic testing facility. It is an open-jet Göttingen-type wind tunnel capable of running at speeds of up to 65 m/s and optimized for noise measurements at frequencies above 250 Hz. The nozzle is 1.2 m high by 0.8 m wide. The free-stream turbulence level is estimated to 0.3%. The AWB has been in service since the 1970s and is used to conduct research on a wide range of topics, from classical airframe noise problems to propeller/rotor noise, as well as jet installation noise and noise shielding problems. The AWB is equipped with most standard means for the realization of acoustic measurements, as well as basic aerodynamic measurements. Extensive details regarding the characteristics of the AWB can be found in ref. [10].

A special rig was designed to extend the capabilities of the facility to meet the requirements of simultaneous aeroacoustic measurements of multiple rotors under static and flight conditions. The main objective of the selected mechanical design is to enable the investigation of the effect of flow and shaft angle on the acoustic radiation of a broad range of propeller configurations; isolated, coaxial, and tandem with vertical and lateral offset, e.g., Fig. 2. The dimensions of the AWB test section allow the investigations of rotors with a diameter of up to approximately 0.4 m. The rig is designed to allow shaft angle variations in the range $\alpha \pm 30^\circ$ and testing at free-stream velocities up to $U_\infty = 30$ m/s.

Above $U_\infty = 30$ m/s, a visual monitoring of the rig showed very noticeable vibrations of the complete assembly. The quantitative effect of these vibrations on the load measurements was increased fluctuations amplitude over the duration of observation. This effect was not, otherwise, documented. The impact of such vibrations on the acoustic radiation cannot easily be quantified, as this would require the synchronous acquisition of pylon acceleration data. Such

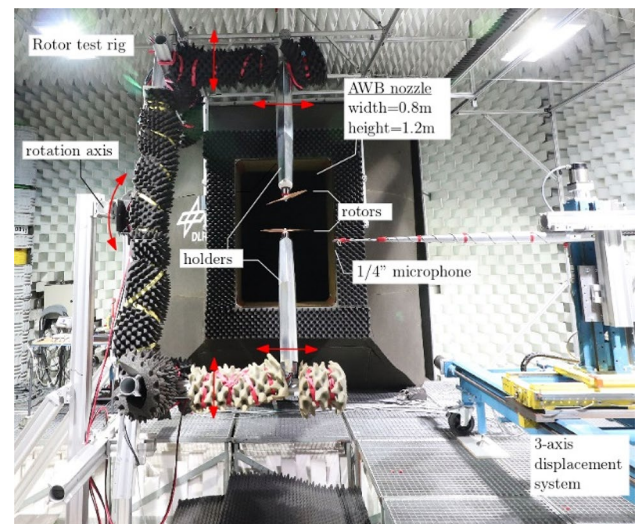


Fig. 3 Full test rig and microphone setup installed in the AWB's test section. Center: coaxial configuration

data was not available in the experiment. As such, it was decided to operate the rig in a regime where no vibrations could be visually identified.

2.2 Rig (pylon) model

Details of the support or rig (pylon) mechanical design and load cell motor assembly and numerical model are provided in Fig. 4. Details of the pylon profile sections are provided in Fig. 5. The pylons have a symmetrical Joukowski airfoil section of variable chord length. This airfoil shape was chosen based on earlier experience in wind tunnel experiment, which showed no flow separation for the Reynolds number range considered herein. In fact, there were no issues related to laminar flow separation tonal noise. The lower part of the pylon has a constant chord length of $c = 200$ mm up to

Fig. 4 Mechanical setup details of the support or rig; left: isometric view of the internal mechanical installation details; right: numerical model used in the simulations

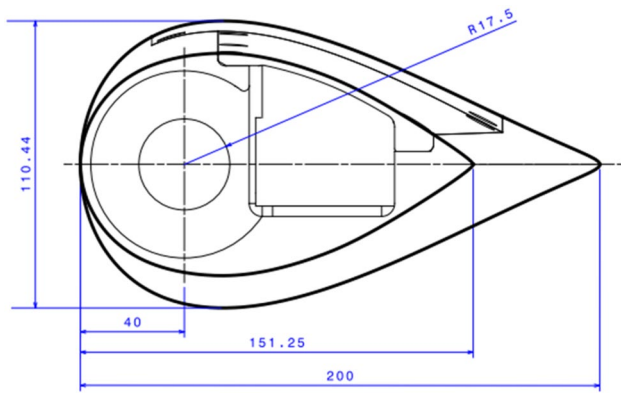
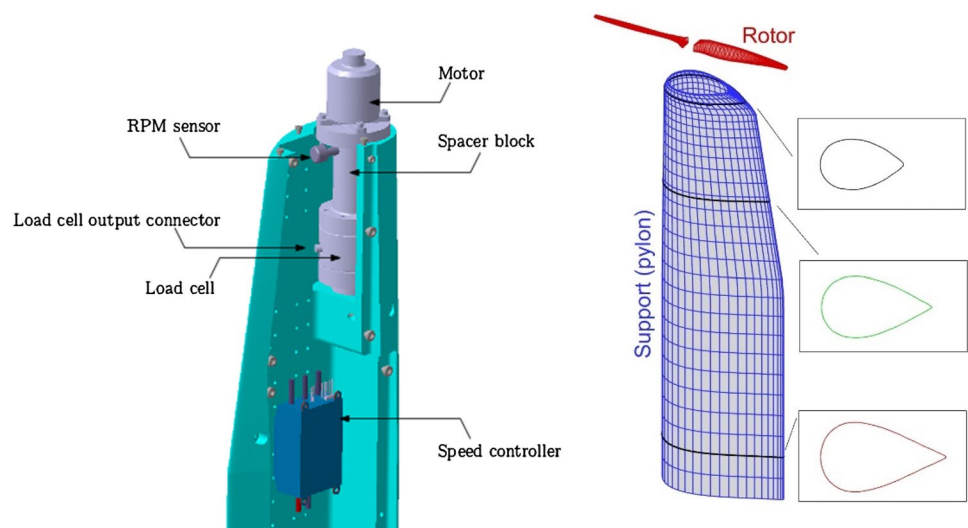


Fig. 5 Pylon profile sections details and dimensions

$z = 524.5$ mm from the fixation plate, at the lower end. From $z = 524.5$ mm upwards, the profile section chord linearly decreases to $c = 151.25$ mm. This was done to minimize flow interference in the vicinity of the propeller. The rotation axis of the propeller is located 40 mm downstream of the pylon leading edge. The pylons were CNC-machined out of solid aluminum blocks and each weigh 14 kg. This large mass helps in dampening flow-related and rotor-related vibrations.

Two coordinate systems are defined in Fig. 6 for the single rotor configuration, the coaxial and tandem configurations. The (x_0, y_0, z_0) axes correspond to the wind tunnel fixed coordinates, while the (x, y, z) axes are body-fixed coordinates. The shaft angle of the propeller defines the rotation between both coordinate systems. Depending upon the

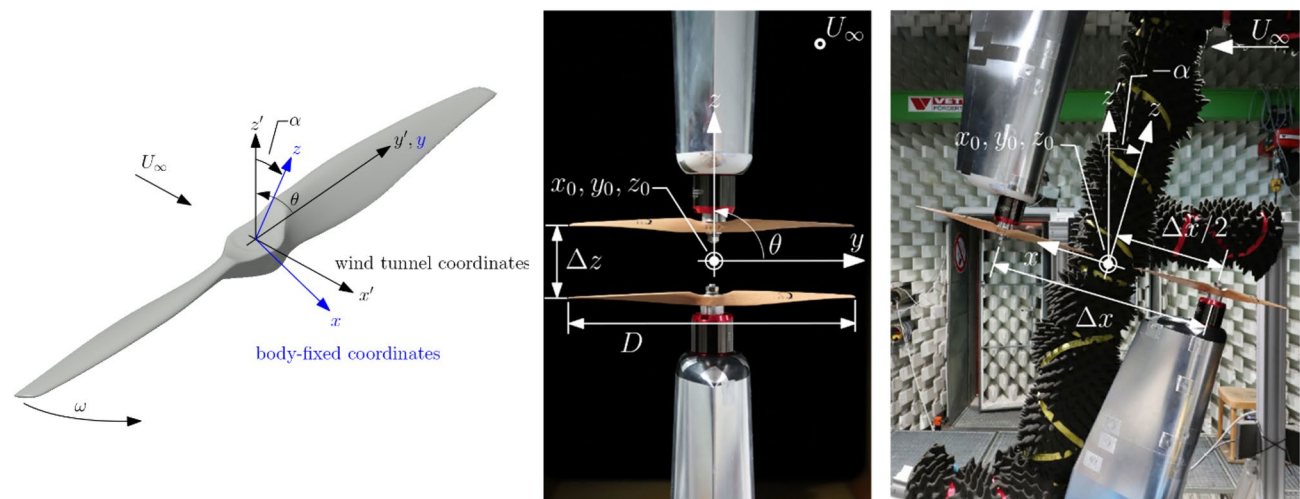


Fig. 6 Coordinate system definition for the isolated rotor (left), coaxial (center), and tandem (right) configurations

configuration considered, a different origin for the coordinates systems is defined. For the single propeller configuration, the origin is set on the rotor axle at the blade tip level in z . For the coaxial configuration, the origin lies at middle point between each rotor in z , centered on both axes in the x - y plane. For the tandem configuration, the origin lies at the mid-point between both rotor axle in x and $y=0$ m with $z=0$ m leveled with the front rotor blade's tip height.

The rig installation allows for lateral spacing settings in the range $\Delta y \pm 0.15$ m, streamwise spacing settings in the range $\Delta x \pm 0.3$ m, and vertical spacing settings in the range $\Delta z \pm 0.3$ m. These setting values are evidently valid for the current set of propellers considered herein. The whole structure of the rig is based on standard X-95 rails and carriers. This choice allows for easy changes in configuration. The rig is fixed to a rotating axle at its center point, i.e., on the left-hand side of Fig. 3 to allow variations in rotor shaft angle.

2.3 Rotor

Several sets of the rotor are tested. For current paper, the test results from a two blade 13×7 rotor are chosen for comparing with the numerical simulation. The rotor 13×7 represents a rotor with 13 inch or 0.33 m in diameter and 7 inch in pitch. The rotor pitch is defined here as the distance the rotor would move forward in one rotation if it were moving through a soft solid. Details of the planform and section profiles of the rotor (13×7) are given in Fig. 7. The rotor is a commercially available one. The blade geometry was 3D scanned, but due to the accuracy of the optical scanner and the manufacture of the blade, the geometric difference of the two blades cannot be avoided. A close inspection on the scanned blade shows that the two rotor blades have a slightly geometric discrepancy. The influence of the geometric difference in the blades on the acoustic results is studied.

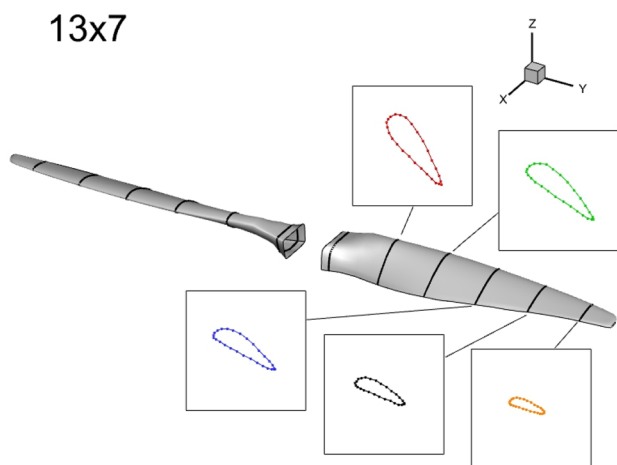


Fig. 7 Rotor (13×7) (in right-handed rotor (RHR) configuration)

The rotors are propelled by Leopard LC5065 motors coupled to YGE 205HVT speed controllers and SM300-Series 3300 W DC power supplies. This combination allows RPM up to 13,000 to be reached. For each rotor, performance data, in terms of thrust and torque, are acquired through miniature six-components load cells, Modell K6D40 from ME-Meßsysteme GmbH, mounted directly underneath the propellers. Each rotor RPM is acquired through a 1/rev signal generated by a Hall-effect sensor mounted to the rotor's shaft. This signal also serves as a trigger signal for data post-processing. The flight conditions include hover, climb, and approach for different flight speeds.

2.4 Aerodynamic and acoustic measurement

For each rotor, performance data, in terms of thrust and torque, are acquired through miniature six-component load cells, Model K6D40 from ME-Meßsysteme GmbH Germany, mounted beneath the motors. The load cells are separated from the motors by an aluminum block spacer to reduce as much as possible the influence of temperature variations and that of the motor's electromagnetic field on the measurements.

The load cells are strain-gauge-based instruments which measure three orthogonal forces (F_x , F_y , F_z) and three orthogonal moments (M_x , M_y , M_z). The load cells were factory calibrated by the manufacturer to a full-scale thrust $F_z = 200$ N ($F_x = F_y = 50$ N) and a full-scale torque M_z of 5 Nm. The load cell signals are sampled at a rate of 5 Hz by the manufacturer-provided pre-conditioning amplifier box. The manufacturer's data sheet rates the load cell with a precision of 0.2% full-scale, corresponding to 0.4 N. Preliminary investigations have shown that this value is strongly dependent on temperature variations and is also RPM dependent, i.e., load dependent. A conservative estimate of the bias error on the load measurement is 0.5% full-scale, though in the experiment, this error was minimized through frequent zeroing of the load cells and short measurement time. The precision of the load cells is within the range given by the manufacturer (i.e., 0.2% full-scale).

The rotor's acoustic emission was acquired through a single 1/4" Brüel und Kjær 4136 pressure field microphone mounted to a three-axis linear displacement system, e.g., Fig. 3. The microphone was placed in the flow field with its membrane protected by a Brüel und Kjær nose cap. The microphone was aligned parallel to the flow field with its sensing surface pointing upstream. The selected measurement positions are depicted in Fig. 16 for a isolated rotor case. The acoustic signal, along with the 1/rev signal, is sampled at a 100 kHz rate on a GMB Viper GmbH 48 channel data acquisition unit. A high-pass digital filter is used to remove low-frequency noise contamination due to the wind tunnel flow. The filter characteristic is removed in the

data processing steps. The processing takes advantage of the 1/rev signal to phase-lock the data on a revolution per revolution basis prior to spectral and time-domain analysis. Each data block is normalized to a unit revolution time to account for fluctuations in total revolution sample count. The typical standard deviation of the sample count per revolution is on the order of 1 to 2 samples, i.e., $10\ \mu\text{s}$ to $20\ \mu\text{s}$, depending on the configuration and RPM, with lower RPM showing smaller variations. Prior to Fourier analysis, 32 individual blocks, i.e., revolutions, are stacked together to form a sufficiently long time series to achieve a high-frequency domain resolution. Each time series is then Fourier transformed using a Hanning window to minimize spectral leakage issues. Averaged spectra are obtained through ensemble averaging of individual spectra and through time-domain ensemble averaging prior to the Fourier analysis step. Spectral averaging preserves the broadband content of the signals, whereas time-domain averaging tends to reduce it due to its incoherent nature and thus emphasize the harmonic components. Further details about the aerodynamic measurements, signal-to-noise ratio considerations, as well as an evaluation of the useful frequency range are provided in [11].

3 Description of methodologies applied in numerical simulations

The aeroacoustic computation into the far field is split into two steps: In a first step, the aerodynamic pressure data on the source surface or perturbation nearfield around the source surface are computed by either high or mid-fidelity aerodynamic tools; in a second step, the sound propagation into the far field is calculated with an acoustic code using aerodynamic input.

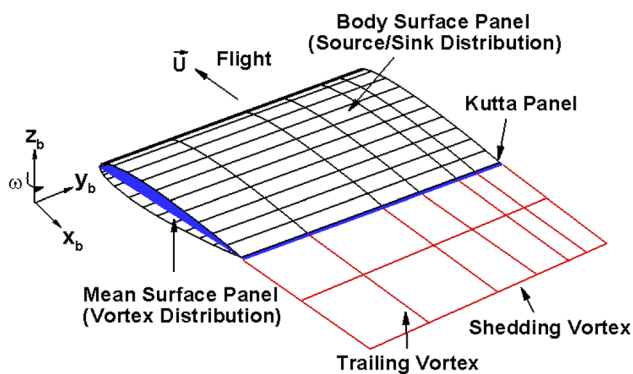


Fig. 8 Numerical model of a blade and wake

3.1 Mid-fidelity aerodynamic tool, UPM

UPM [12–16] is a velocity-based, indirect potential formulation—a combination of source and dipole distribution on the solid surfaces on the rotor or wing surface and dipole panels in the wake, as shown in Fig. 8. A short zero-thickness elongation of the trailing edge along its bisector, called Kutta panel, ensures the flow tangency condition at the trailing edge and defines the total strength of the circulation at the blade section. An iterative pressure Kutta condition is implemented to subsequently ensure pressure equality at the trailing edge. This method is proved to be computationally efficient and robust with respect to the size of the chosen time step and the number of panels on the blade.

The pressure on the blade surface is calculated from the unsteady Bernoulli equation. The compressibility effect is only considered in computing the normal force coefficient by applying Prandtl–Glauert correction. The free wake is represented in the form of connected vortex filaments and is released from the downstream edge of the Kutta panel. The spanwise variation of the circulation on the wake panels is the same as that on the Kutta panels and is kept unchanged throughout the whole computations. The wake can also be represented in the form of vortex particles as UPM is linked to a particle solver originally coded for the DUST-panel method [17] by the Politecnico di Milano. The particle wake method promises an improved simulation robustness for cases where straight line vortex filaments would cross solid body surfaces. To accurately predict blade–vortex interaction (BVI), especially parallel BVI, a hybrid method combining the wake panel model and particle model can be applied.

In the current implementation, the pylon support is not considered as a lifting surface and thus contribute zero net vorticity to the flow. To model the presence of the pylon, potential theory in form of a panelized pylon, as shown in Fig. 4 right, is used. In this model, the pylon surface is discretized into a system of quadrilateral panels. Each panel is represented as a source/sink of constant strength. The velocity at any panel centroid is then given

Table 1 UPM resolution

Panels per airfoil section	56
Radial number of panels per blade	29
Total number of panels per blade	1624
Number of pylon panels	1470
Time step size	2 degree
Forward flight	5 degree
Hover (isolated rotor)	2 degree
Hover (coaxial or tandem)	
Number of revolutions	4 to 6
Forward flight	8 to 16
Hover	

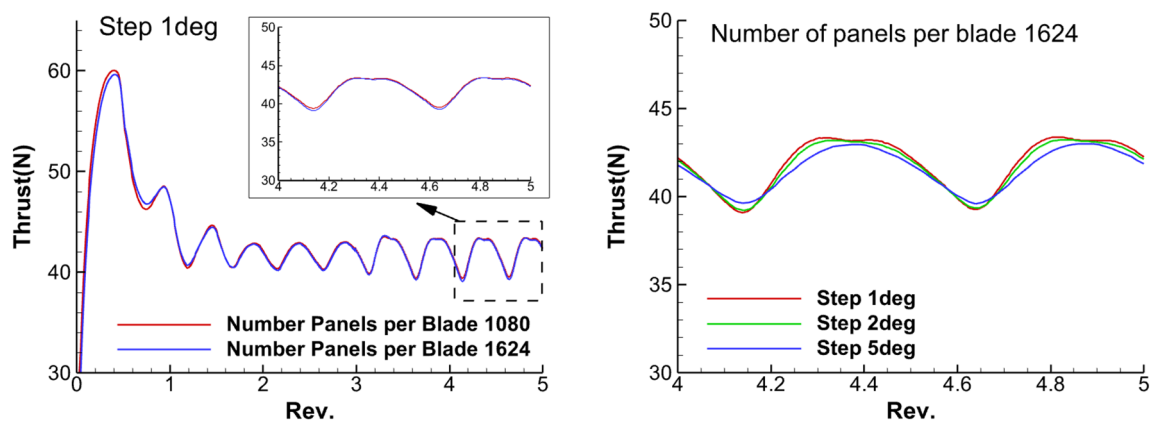


Fig. 9 Rotor thrust convergence study for a forward flight. Left: thrust as function of panel resolutions at given time step; right: thrust as function of time resolutions at given panel numbers

by the sum of the influences from the rotors, wakes, and pylon itself together with the free-stream component of velocity. A boundary condition of zero penetration is enforced simultaneously at the centroids of all panels. The specific number of panels on the blade and pylon utilized in this paper are listed in Table 1. The numbers derived according to convergence of the code results. One criterion is to check the thrust variation as a function of blade panel numbers and time steps. The results of Fig. 9 show the rotor thrust convergence study for a forward flight. The number of panels on the blade used in the current paper derived a very good convergent result, as shown in Fig. 9 left. In addition, the right step size in the simulation can assure to capture the right aerodynamic interaction behavior. The amplitude of the thrust peaks and their shape at different time steps appears to approach a periodicity state after 4 rotor revolutions and almost same behavior is obtained for time step less than 2 deg. An alternative approach for the convergence study is to compare the pressure distribution at different spanwise sections with test or CFD data.

It is possible in UPM to activate an approximate boundary-layer (BL) analysis [16] for lifting and non-lifting bodies. Various simple integral methods for laminar/turbulent BL analysis are employed for predicting the BL. The laminar and the turbulent separation criteria are part of the integral methods (usually based on shape factor values). The analysis is based on sectional flow properties easily defined thanks to structured panel surfaces in UPM. Instead of defining laminar and the turbulent BL according to the integral methods, the BL transition can also be set at a fixed chordwise position using a tripping marker. Two methods are available for separation region estimation, simple angle criterion and turbulent

Stratford method. In simple angle criterion, flow separation is assumed to occur if the flow is retarded. In the current paper, simple angle criterion is applied. If flow separation is predicted, the boundary-layer analysis ends immediately at the separation point. The BL analysis is performed as a pure post-processing step based on the inviscid potential flow solution. The results are not fed back to the potential flow solver to account for the displacement of the outer inviscid flow. Therefore, there is no correction on the blade surface pressure.

3.2 High fidelity aerodynamic tool, CFD TAU

The unstructured CFD code TAU is based on the solution of the Reynolds-averaged Navier–Stokes equations on hybrid unstructured meshes. The solver relies on a cell vertex scheme to discretize the mass, momentum, and energy fluxes [18]. In the current paper, the second-order accuracy central scheme was used for spatial discretization. Scalar dissipation has been used as the central dissipation scheme. The temporal discretization is based on an explicit Runge–Kutta scheme. As turbulence model, the two-equation turbulence model Menter SST was used. Furthermore, all surfaces were simulated fully turbulent. To accelerate the simulation, full multigrid was applied. Steady-state simulations were performed and six orders of magnitude convergence were ensured for each simulation.

The mesh for the simulations was created starting from a scanned blade surface and is built entirely with hexaeder. The mesh has a mesh count of 34 million mesh points. The entire propeller was meshed including both rotor blades and the connecting hub. 214 mesh points were used in the air-foil circumference and 234 mesh points were used along the span. The far field is located about 116 rotor diameters

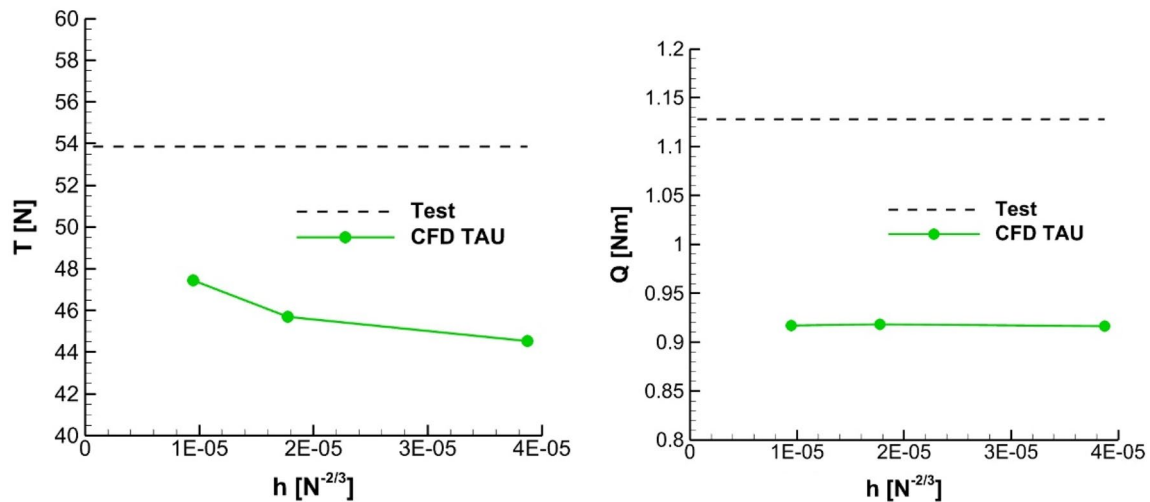


Fig. 10 Mesh convergence studies for 13×7 rotor at 12000 rpm

from the propeller and is realized from propeller surface to far-field edge with 176 mesh points. The y^+ value is below the value 1 over the entire surface.

In the lead-up to this mesh, a mesh convergence study was first carried out. Meshes with a number of mesh points of 4 million, 13 million, and 34 million were investigated for a speed of 12,000 rpm. Care was taken to ensure that all meshes have a uniform mesh topology. Figure 10 shows the result of the mesh convergence study. The thrust and moment are plotted against the cell width in Fig. 10 left and right, respectively. It can be seen that as the cell width decreases, the thrust converges consistently toward the wind tunnel experiment value. For the moment, there is no significant change when the cell width is decreased. Due to the lower thrust compared to the experiment, the moment is also smaller than in the experiment. The difference between simulation and wind tunnel results have not yet been further investigated. Due to this fact, it was decided to perform all further simulations with the 34-million-point mesh and not to perform any further mesh refinement.

3.3 Vortex core radius and aerodynamic trim computation

For mid-fidelity UPM aerodynamic simulations, an inviscid and potential flow is assumed. In UPM, the wake dissipation is realized using a vortex core radius model. The various vortex core model, such as Rankine, Kaufmann–Scully, etc., can be used. In general, for a given vortex model, a large vortex core radius can decrease the averaged inflow downwash velocity as a weak-induced velocity from the free wake system is generated, and therefore, large rotor thrust is obtained as a consequence of a higher effective blade angle of attack.

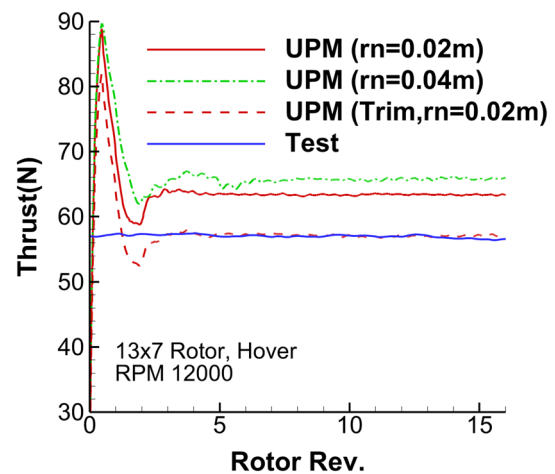


Fig. 11 Rotor thrust as a function of rotor revolutions and vortex core radius

This phenomenon is demonstrated in the rotor thrust time histories for the 13×7 rotor (Fig. 7) at RPM 12000 in hover condition, as shown in Fig. 11. For comparisons, the AWB test data are also plotted. As expected, the thrust level for the large core radius ($rn=0.04$ m) for a Rankine vortex model (red dashed line) is higher than that of a core radius $rn=0.02$ m. For a given vortex model, the choice of a proper vortex core radius is a key to determine the proper induced inflow velocity for the rotor. In the current simulations, the Rankine vortex model with a core radius $rn=0.02$ m is used in the following simulations.

To have a fair comparison for noise emission between experimental data and numerical simulations, the trim condition between the numeric and experiment should be matched. Therefore, a trim to the measured thrust is applied.

Here, the flow conditions, such as rotor shaft, advance ratio, and RPM, are fixed. In general, there are two ways which can be used to change simulated thrust value, adjusting vortex core radius as demonstrated in Fig. 11 and adjusting blade pitch control angle. Here, a fixed vortex core radius as $r_n = 0.02$ m is used to assure a good stability of the wake development. A force trim according to the rotor thrust from the test is used. The blade pitch control angles are determined by the trim algorithm in such a way that the thrust matches the experimental value in a given tolerance, as shown by the red dashed line in Fig. 11. For this trim example, a pitch decrease of about 1.62 deg is required to match the experimental value.

In the rotor/rotor interaction cases, the trim procedure is then applied to both rotors simultaneously to consider the multi-influence of rotors.

3.4 The aeroacoustic model

The Aeroacoustic Prediction System based on an Integral Method, APSIM, has been developed at the DLR Institute of Aerodynamics and Flow Technologies (DLR AS) for the prediction of rotor or propeller noise radiation in the free field. The method is designed to calculate wave propagation over large distances in uniform flows. The methodology is based on the Ffowcs-Williams/Hawkings (FW-H) formulation for porous and blade surfaces. Only linear sound propagation is considered. In this study, the blade surface pressure data computed by UPM or TAU are used as input for APSIM. The calculations, performed in the time-domain, deliver a pressure time history at any desired observer location, which can be Fourier analyzed to derive acoustic spectrum data. APSIM has been extensively applied for the aeroacoustic analysis of a wide range of helicopter and propeller configurations, and in recent times, the coupling of the code to the CFD solver TAU has been matured and automated to a great degree.

To evaluate the rotor noise shielding effects by the support pylon, a Fast Multipole Boundary-Element Method (BEM) which solves the exterior Helmholtz problem for the scattered pressure field is used [19, 20]. It is a BEM method which employs the Fast Multipole Method (FMM) for triangulated surfaces. An iterative solver from PETSc library [21] as well as OpenMP/MPI parallelization for the fast evaluation of matrix–vector products are applied, so that no storage of the matrix is required. In addition, the Burton–Miller approach is used to guarantee the uniqueness of the solution. Based on the assumption of low Mach number potential flow, a Taylor transformation of the convected wave equation into the Helmholtz equation is used to consider the mean flow effect.

4 Results for the isolated rotor

The rotor 13×7 (Fig. 7) is chosen for the UPM simulations. A total of 16 rotor rotations for hover and 6 rotor rotations for forward flight were computed to obtain a fully periodic solution. In hover, the wakes are transported only by the induced velocity and, but not by some on-flow velocity. Therefore, a longer computation is required to get rid of the influence from the starting vortices.

The computation proceeded in azimuthal steps of 5° for the hover and 2° for the forward flight. Each blade was discretized in the present study by 56 planar surface elements (panels) along the profile contour and 29 panels along the span. A half-cosine spacing was used along the blade span. The details of the numerical discretization are listed in Table 1.

4.1 Hover at RPM = 8000, 10,000, 12,000

4.1.1 Trim conditions

The collective pitch correction as well as the achieved rotor thrust are summarized in Table 2 and Fig. 12 left for different rotor RPM. The correction on blade pitch angle ($\Delta\delta$) here in Table 2 represents an addition angle added to the blade to achieve the thrust value (T) obtained in the test. A negative value means a reduction on the pitch angle. The thrust matches the experimental value in a given tolerance within 0.5 N. A comparison of an averaged thrust as a function of the rotor speed is also given in Fig. 12 (right).

The thrust time history from the trimmed UPM simulations shows that with the start of the rotor revolution, the thrust in the simulation increases steeply and then settles down to a fairly constant value after some revolutions and matched with the test value. This thrust build up is due to the strong starting vortex which is shed off the blade trailing edge at the impulsive start of the rotor. With the progress of the computation, the starting vortices move away from the blades and the normal wake structure, which is relevant for the practical situation, develops as demonstrated by the fairly constant thrust values. A comparison of non-trimmed time-averaged thrust (Fig. 12 right) indicates that general tendencies captured in the measurements are reproducible using all computational tools; however, some differences can

Table 2 Trim conditions (Hover)

RPM	M_h	$\Delta\delta(\text{deg})$	T(N)	T(Test,N)
8000	0.41	– 1.08	24.4	24.7
10,000	0.51	– 1.11	39.6	39.8
12,000	0.61	– 1.62	57.5	57.2

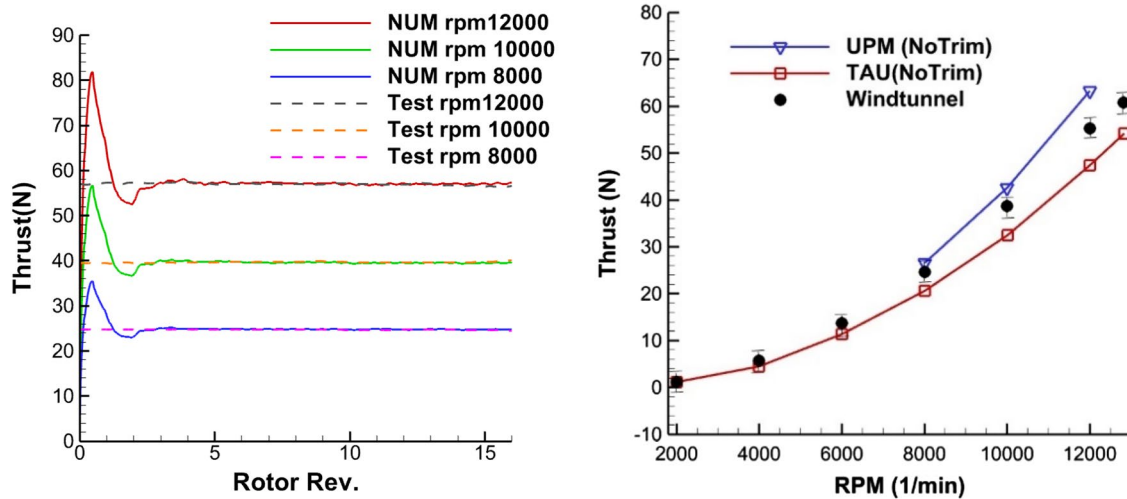


Fig. 12 Left: trimmed rotor thrust as function of rotor revolutions; right: results for varying rotor RPM

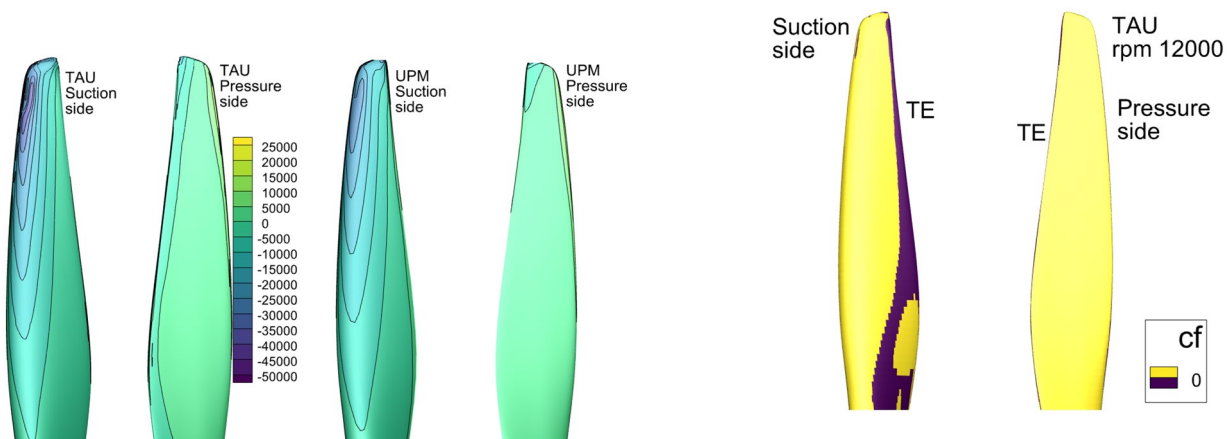


Fig. 13 Suction and pressure side distribution of the $p-p_0$ for TAU and UPM at rpm 12,000

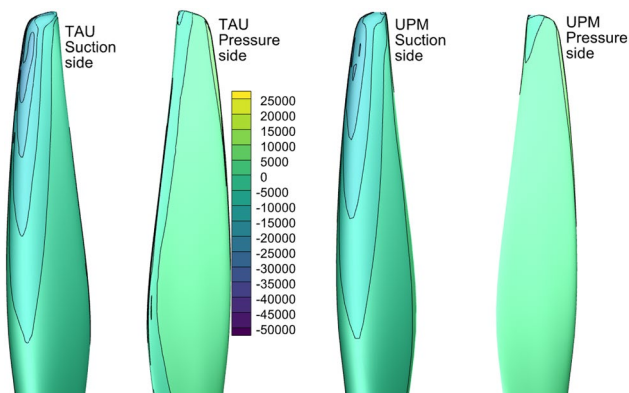


Fig. 14 Suction and pressure side distribution of the $p-p_0$ for TAU and UPM at rpm 10,000

Fig. 15 Separation region (blue) predicted by CFD TAU for rpm 12,000

be noticed. The difference increases with increasing RPM. The overprediction of thrust values from potential flow solvers is observed when trim is not applied.

4.1.2 Aerodynamics

The comparison of the blade surface pressure distribution represented as $p-p_0$ (unsteady surface pressure) between TAU and UPM is given in Figs. 13 and 14 for RPM 12000 and 10,000, respectively. The p_0 is air pressure in undisturbed medium. The $p-p_0$ distribution between TAU and UPM resembles very good correlations in terms of pressure pattern and amplitude in both suction and pressure side. The difference mainly occurs in the trailing edge area, especially toward the blade root region where a large flow separation region is observed in the TAU simulation as indicated by separation region (blue) predicted by CFD TAU shown in

Fig. 15. However, UPM solves only the potential flow and no viscous effect is predicted. According to the source of the broadband noise, the occurrence of the flow separation can be used as indicator on the increasing of the broadband noise which is observed in the test.

Similar characteristics in terms of $p-p_0$ distribution are also observed for RPM 8000 which are not shown here.

4.1.3 Acoustics

The FW-H impermeable surface approach uses blade surface data as input. For this approach, only the surface pressure time histories are needed, and hence, only noise contributed from monopoles (thickness noise) and dipoles (loading noise) can be included. In the present study, the unsteady pressure data on the rotor blade are used as input to APSIM. The presentation of the acoustic results will focus on data taken in the test on a polar arc represented by microphones from number 5 to 11 as defined in Fig. 16 (left). The arc is located in the X-Z plane with the arc radius of 0.3 m and

polar angle difference of 15° . The microphone 9 is located in the rotational plane (X-Y), where $Z=0$. Results will be presented in terms of overall sound pressure level (OASPL) directivities and spectrum.

It has to be mentioned that in UPM simulation, only scanned geometry of the blade 1 is used and the geometry of another blade is copied directly from the blade 1, while in TAU simulation, the scanned geometry of two complete blades is directly applied. To check the influence of the geometric difference of two blade mentioned in the previous section, the acoustic results in terms of time histories and the spectra using TAU and UPM input are first compared, as shown in Fig. 17. Figure 17 (left) shows a comparison of the predicted sound pressure time history at microphone 9 for both thickness and loading noise. The thickness noise (Mono) from the blade 1 for two predictions are perfectly meet, while the difference in peak value for blade 2 indicates the influence of geometric discrepancy on the thickness noise. The slight difference in peak value between blade 1 and blade 2 is less than 1 pa. Similar peak difference in the

Fig. 16 Microphone positions (left) for the isolated rotor (right) case

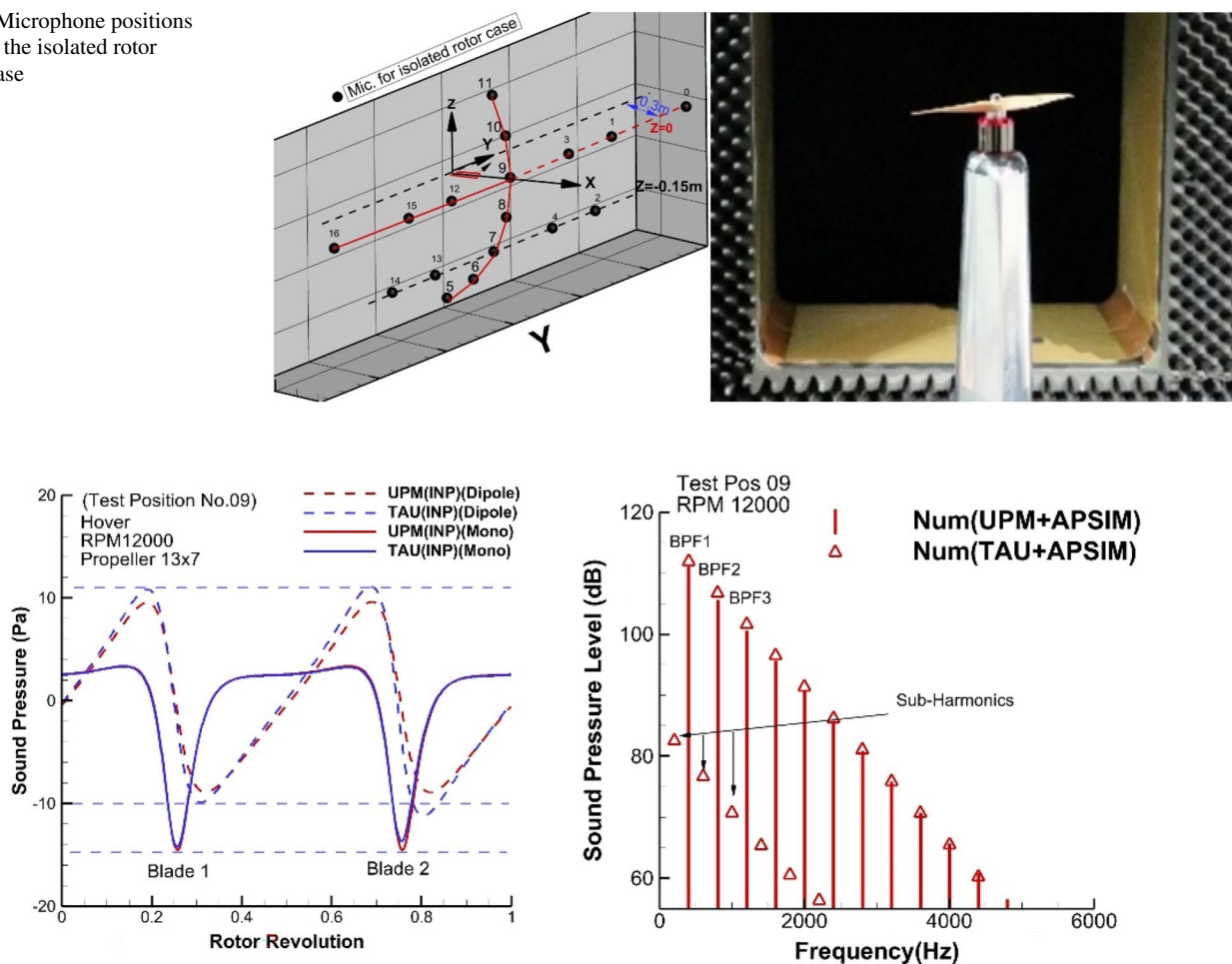


Fig. 17 Influence of geometric difference on the acoustic results: time history (left); spectrum (right)

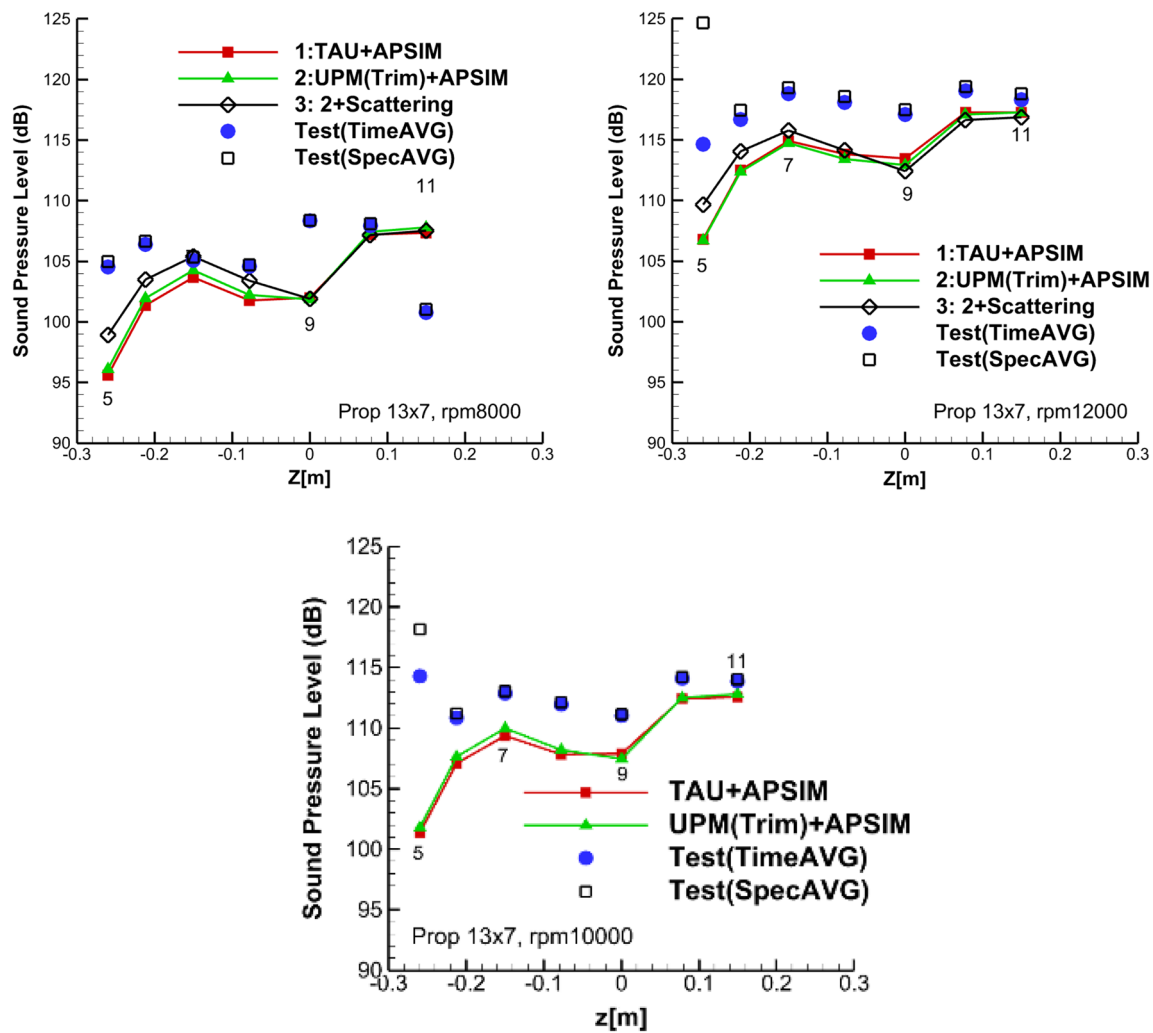


Fig. 18 Polar directivity for OASPL at polar microphone from 5 to 11. Comparison of predictions with measurements [11]

loading noise (dipole) using TAU input is also observed. The deviation of the loading noise between two predictions is mainly caused by the difference in the methodology where no viscous effect on the blade pressure was considered in UPM. Otherwise, the correlation between the two simulated time histories is very good. Figure 17 (right) compares predicted sound pressure spectra for two simulations. The influence of blade asymmetry can be identified by the additional subharmonics among two BPFs appearing in the results using TAU input. In general, the level of the subharmonics is more than 25 dB lower than the level of the BPFs and their contribution to the overall sound pressure level can be neglected.

The polar directivity for the OASPL is shown in Fig. 18 for the 13×7 rotor and 3 different RPM. Experimental data as well as simulation results from UPM and TAU are presented. The rotor noise shielding effects by the support pylon were also evaluated for RPM 8000 and RPM 12000 marked

as the value 3 in the plots. In addition, the OASPL obtained from the experiment using two different averaging techniques is included. As mentioned in the previous section, the advantage of the time-averaged noise spectrum is that the random or stochastic noise, such as broadband noise or flow noise with non-periodicity behavior, can be removed or reduced dramatically. Therefore, the difference between spectrum averaging method and time-averaging method can provide an estimated of the non-harmonic source contribution.

In general, the contribution of the broadband noise to the OASPL is negligible in the measurement results for all the microphones except microphone five. For microphone 5 at RPM 12000, the OASPL (black open square) computed using spectral averaging is significantly higher than the OASPL (blue solid circle) computed with time-averaging. This is because the microphone five is located directly below the rotor and the rotor downwash increases the microphone self-noise. By reducing the rotational speed, the strength

of the rotor downwash is reduced and the microphone self-noise is reduced too. Therefore, the difference between the two averaged data is reduced.

The results of Fig. 18 indicate that the trimming procedure allows the UPM simulations match TAU results. The acoustic simulations are able to capture the experimental trends, especially for the microphone located above the rotor rotational plane. There are in general higher OASPL levels in the measurements for the microphone below the rotational plane and the difference between the numerical and test increases when the microphone moves in the direction toward the microphone 5 (directly below the rotor and toward wind tunnel floor). The difference is partly due to the influence from the acoustic scattering of the pylon support as indicated by the results including the acoustic scattering of the pylon support shown in black line for RPM 12000 and 8000. The simulation of the acoustic scattering from

the rotor support system indicated an influence about 1 to 3 dB on the overall sound pressure of the polar microphones.

Figures 19 and 20 present the acoustic spectrum for the microphone located on a polar arc at positions 8, 9, and 10, which are located below, on and above the rotor rotational plane. The frequency range of the spectrum is limited to 6 kHz for clearness purposes. The useful frequency range of the experimental data exceeds 20 kHz. It should be mentioned that broadband sound and motor noise contributions were not included in the numerical simulation.

The comparison of the spectrum indicates that:

1. For both the simulations and the test, the rotor harmonic sound components are found to dominate at low frequency. Broadband noise becomes more important for frequencies greater than 2 kHz, but the contribution to overall sound pressure level can be neglected.

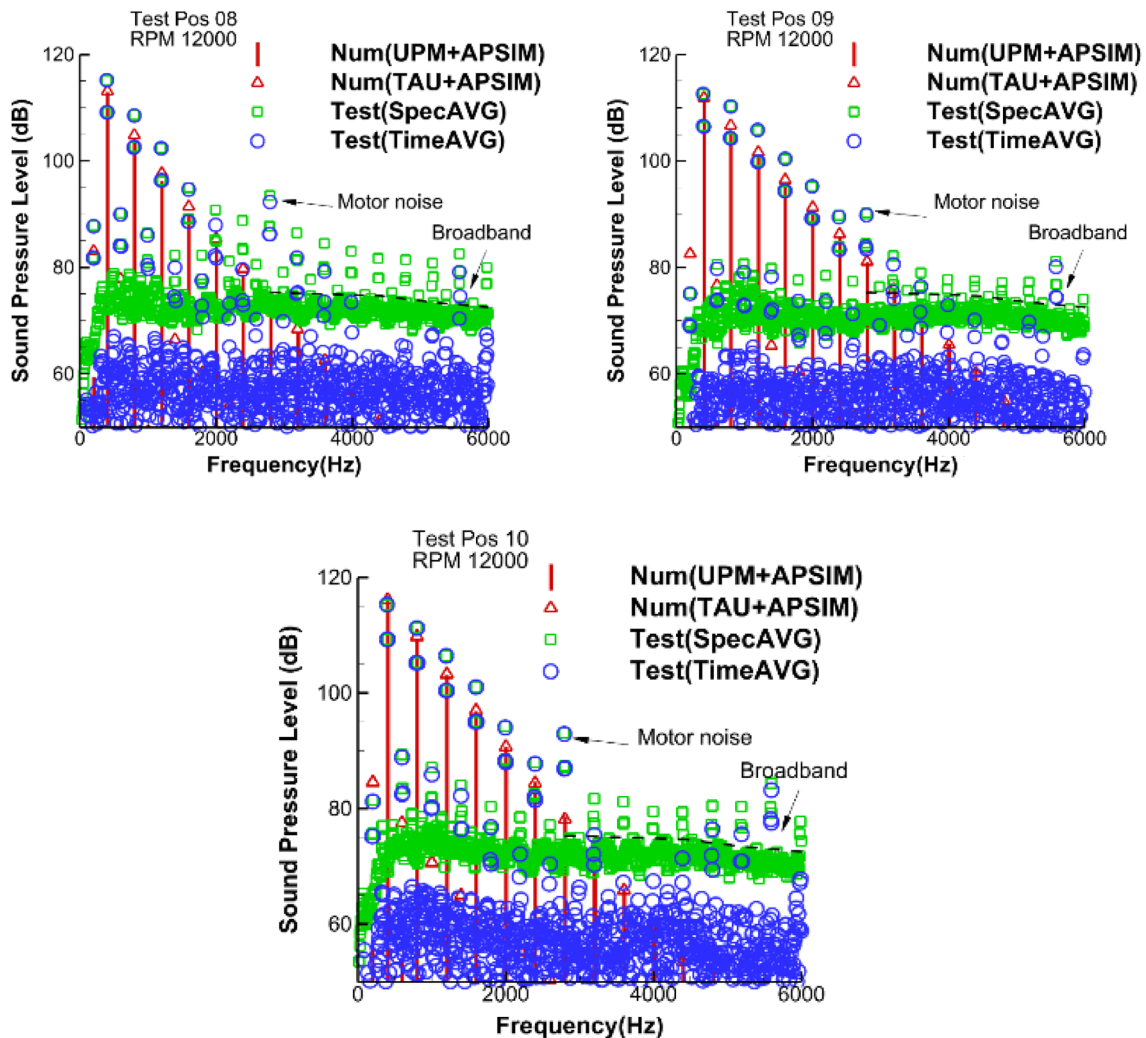


Fig. 19 SPL spectra from microphones 8,9,10 for RPM 12000

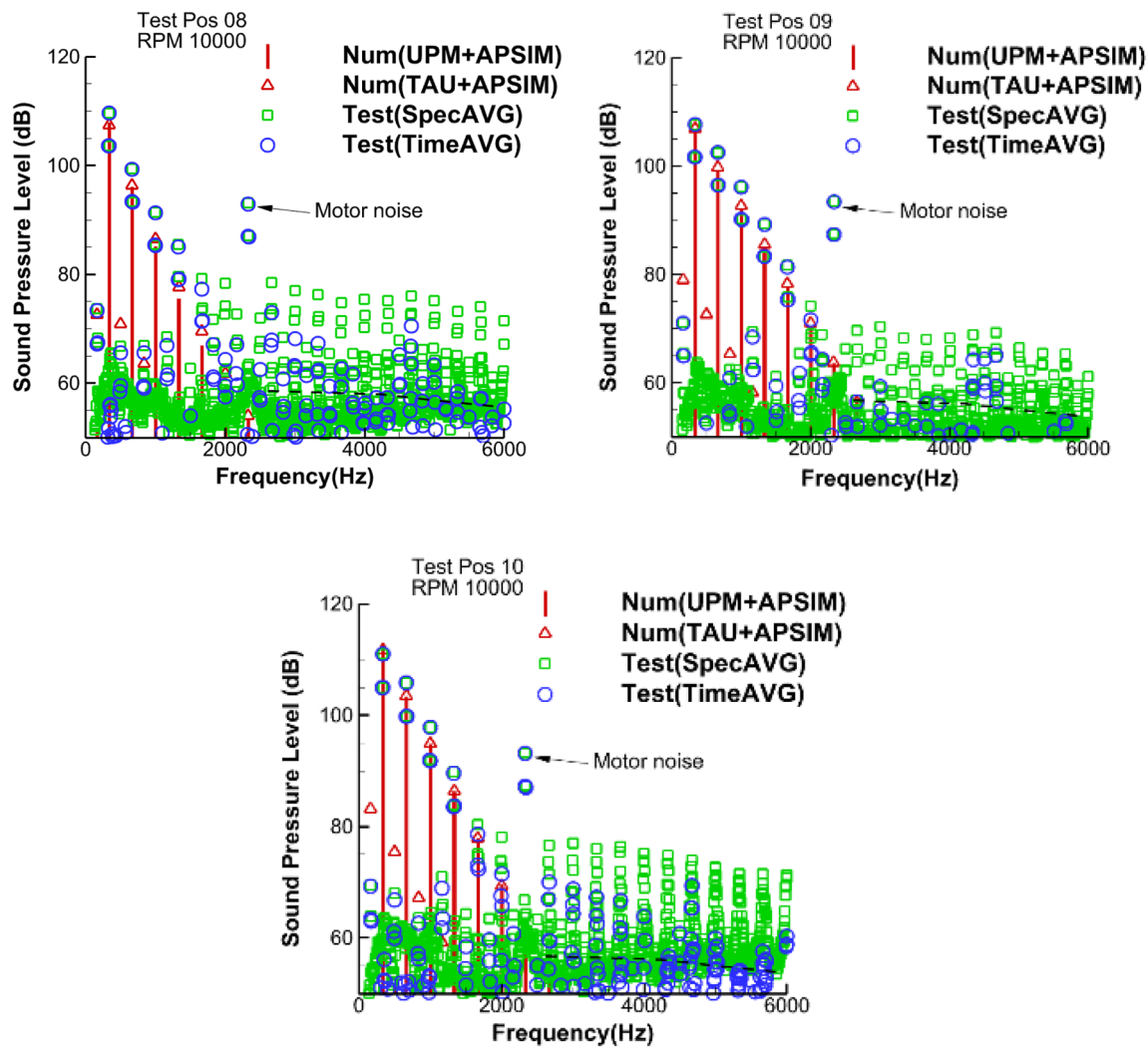


Fig. 20 SPL spectra from microphones 8,9,10 for RPM 10000

- The results using both UPM and TAU input match very well with each other in terms of amplitude of the harmonics and also the experimental trends. The highest level in the spectrum from the simulation is located at the first BPF and decays almost linearly with increasing frequencies; when comparing Fig. 19 with Fig. 20, the decay rate increases with decreasing RPM as a reduction in Mach number and hence in doppler amplification; it is preferable to use as low a rotor RPM as possible to reduce the noise radiation.
- The influence of blade-blade discrepancy can be identified by the additional subharmonics among two BPFs as explained also in previous section in Fig. 17. The subharmonics are also observed in the experiment. For all the microphones, the levels of the subharmonics are much smaller than the levels for the BPFs. The experimental results also show additional subharmonic contributions from the motor.

Table 3 Trim conditions at shaft angle=0

V_{∞} (m/s)	RPM	M_h	$\Delta\delta$ (deg)	T(N)	T(Test,N)
15 m/s	8000	0.41	- 2.12	27.1	26.8
15 m/s	10,000	0.51	- 2.47	40.0	40.0
15 m/s	12,000	0.61	- 3.19	54.7	54.9

- Broadband noise observed at the higher harmonics above 2000 Hz is less important for the total noise.
- In general, motor noise contributes to all the rotor harmonics and its subharmonics, but the motor noise overwhelms the rotor contributions only at specific harmonics, especially for RPM 10000.

4.2 Forward flight at $v = 15$ m/s and RPM at 8000, 10,000, 12,000

For this study, the impact of the rotor RPM on the rotor performance and noise is studied. The rotor shaft angle is kept at 0° .

4.2.1 Trim conditions

The collective pitch correction to achieve test thrust is summarized in Table 3 for different RPM. The rotor thrust increases with increasing the rotor RPM. Similar to the hover condition, a decrease in the pitch angle is observed. In forward flight, more reduction on the pitch angle is required to match the test thrust. A lesser induction from the wake on the rotor inflow is expected, as the wake convects further downstream and away from the rotor.

In forward flight, the blade local flow speed is a vector of the forward flight speed superimposed with the circumferential speed due to rotor rotation. This leads to a variation

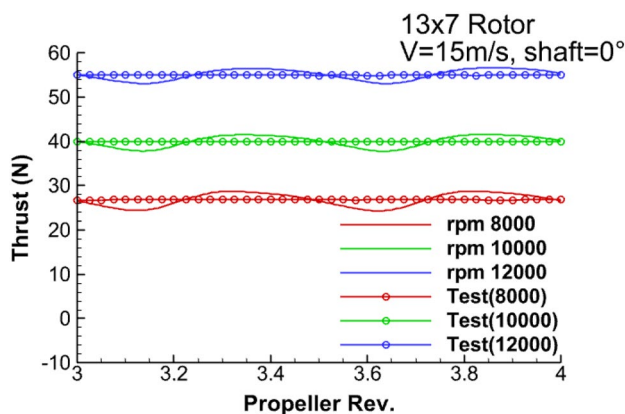


Fig. 21 Rotor thrust as a function of rotor revolutions at different RPM

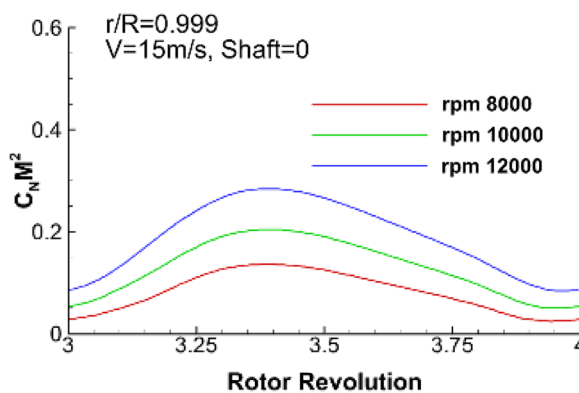


Fig. 22 Time history of normal force coefficient C_{NM}^2 at two tip region sections

of the blade local on-flow. On the advancing blade side, the impact of the free-stream increases the on-flow velocity, and at the retreating side, the on-flow velocity will be decreased. Therefore, due to the fixed blade pitch angle, the blade force on the advancing blade side is increased and decreased on the retreating blade side. This causes a two-per-rev periodic force development in a sinusoidal variation as shown in Fig. 21 for two bladed rotors.

4.2.2 Aerodynamics

Figure 22 plots the development of blade normal force coefficient C_{NM}^2 for different RPM. Higher loads are observed at advancing rotor side of the second and third quadrants of the rotor revolution as fact of the free-stream velocity component to an increase in the effective local velocity. The

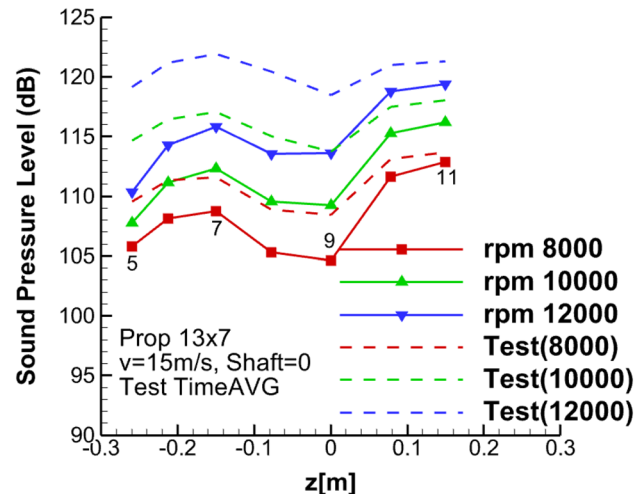
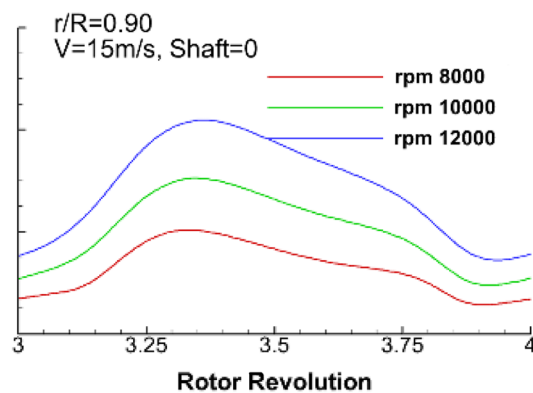


Fig. 23 OASPL polar directivity at polar microphones from 5 to 11. Comparison of different RPM at forward flight



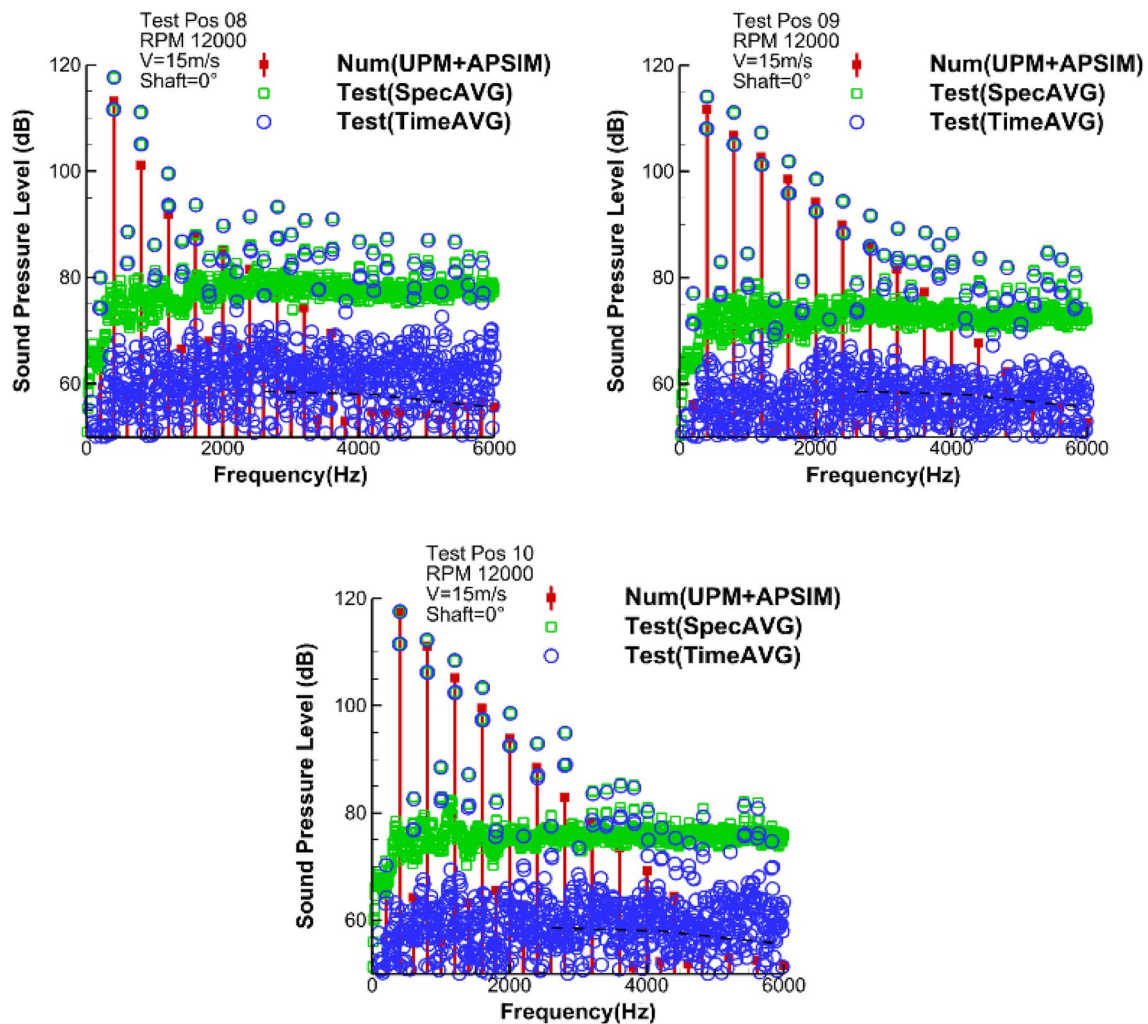


Fig. 24 SPL spectra from microphones 8,9,10 for RPM 12000 at forward flight

opposite effect occurs in the blade retreating side. The one per revolution (1-P) behavior is clearly seen. It is expected that the lift variation in 1-P behavior will contribute to high harmonic loading noise.

4.2.3 Acoustics

A comparison of the OASPL polar directivity is shown in Fig. 23 for different rotor RPM. The dashed lines represent the noise obtained from time-averaged test data, while the solid lines with symbols denote simulation results. The trends with varying microphone position and increased RPM are captured. The numerical simulations in general underestimate the absolute value for all RPM in this flight condition, especially for the microphones below and on the rotor rotational plane (mic. 5–9). A better correlation between simulations and test data is observed for the microphones above the rotational plane (mic. 10 and 11).

The comparison of the spectrum for RPM 12000, as shown in Fig. 24, indicates that for both the simulations and the tests, the rotor harmonic sound components are found to dominate at the low frequency. The highest level in the spectrum from both the simulation and the test is located at the first BPF and decays with increasing frequencies. Comparing with the hover, as shown in Fig. 19, the decay rate of the tone noise is relatively slow in the forward flight, as increasing the unsteady noise. There is increasing broadband noise or background flow noise in the test, but still remaining well below the rotor contribution [11]. Background flow noise is introduced due to the wind tunnel stream but also due to flow interaction with the inflow microphone. This type of noise is not included in the simulations.

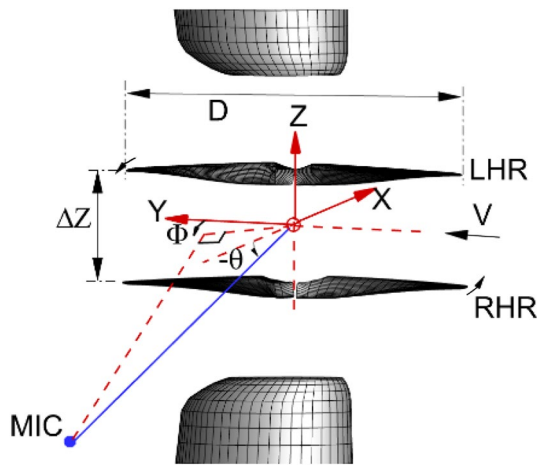


Fig. 25 Coordinate and geometric definition for the coaxial-rotor configurations (side view)

Table 4 Trim conditions (Hover)

RPM	M_h	$\Delta\delta(\text{deg})$	T(N)	T(Test,N)
8000	0.41	RHR: - 0.33	19.9	20.1
		LHR: - 1.17	23.7	23.8
10,000	0.51	RHR: - 0.62	30.8	31.2
		LHR: - 1.14	37.9	38.3

5 Results for two rotors in coaxial configuration

For the coaxial configuration, as shown in Fig. 25, the coordinate system's origin lies at the middle point between each rotor in Z, centered on both axes in the X-Y plane. The distance between two rotors is defined by $\Delta Z/D$, where D is the diameter of the rotor in 0.33 m.

In the simulation, both rotors are identical (same geometry, same geometric pitch) and turn in opposite direction with the same rotational speed. The lower rotor defined as right-handed rotor (RHR) rotates count-clockwise as applied in isolated condition and the upper rotor defined as left-handed rotor (LHR) rotates then clockwise. The starting phase positions of the reference blade for both rotors point toward the downstream ($\Phi = 0$) and both rotors are phase locked. In the test, however, there is no phase synchronization of the two rotors. Due to slightly different RPM of each rotor, the time-averaged data may provide less-relevant results. Therefore, only the spectrum averaged test data are used for the comparisons.

Some numerical results for two rotors with different starting position ($\Phi = 45^\circ, 90^\circ$) will be given to show the effect of the phase delay between the rotors on the aerodynamic interaction and the acoustic interference.

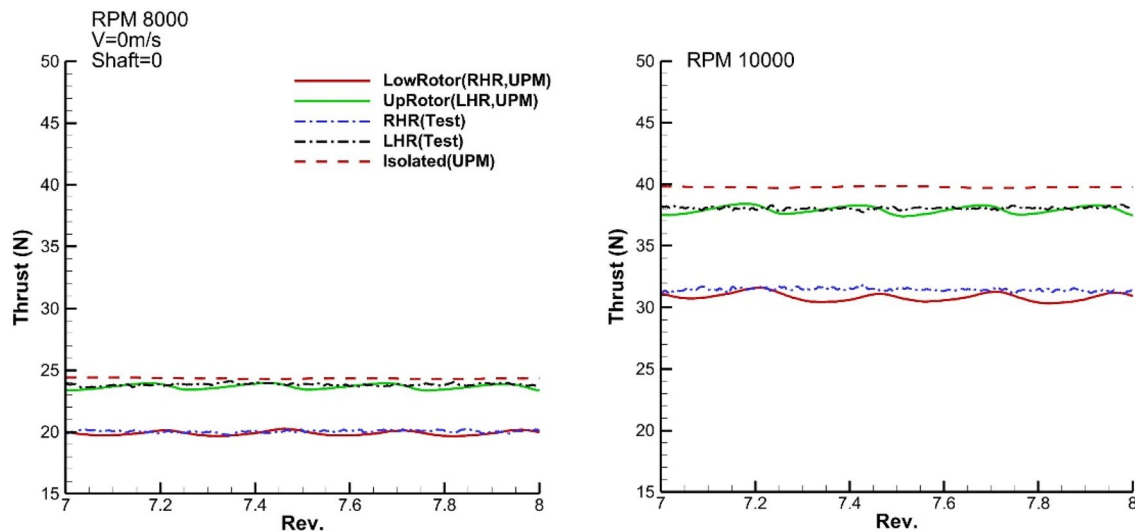


Fig. 26 Rotor thrust as function of rotor revolution

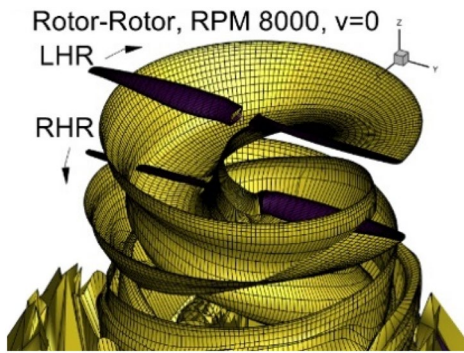


Fig. 27 Snap shot of the rotor wake development under the influence of the rotor–rotor interactions

5.1 Hover at $\Delta z/D = 0.25$ for rotor starting phase positions at $\Phi = 0$

5.1.1 Trim conditions

The collective pitch correction to match the test thrust is summarized in Table 4 for two RPM. The lower rotor (RHR) requires relative less pitch angle correction than the upper rotor (LHR) one to match the test thrust.

The influence of the rotor–rotor interaction in hover condition can be demonstrated first by comparison with the isolated rotor thrust, as shown in Fig. 26. In coaxial configuration, there are two effects contributing to the interactions:

- The multi-inductions of the wakes of both the upper rotor (LHR) and the lower rotor (RHR) cause deformations of the wakes and introduce additional downwash velocity. This reduces the effective angle of attack of both rotors, and therefore reduces the rotor thrust as shown in Fig. 26 for both rotors when comparing to the isolated case. As RHR merges directly inside LHR wakes (Fig. 27), this effect is much stronger for RHR

and increases with increasing RPM. The influence is a function of rotor-to-rotor distance and RPM.

- The rotor potential field (due to pressure) and displacement (due to blade thickness) cause additional multi-inductions among rotors and wakes. This effect introduces 4-per-rev variations with a maximum occurring at the blade position when LHR and RHR overlap.

5.1.2 Aerodynamics

A snap shot of the rotor wake development under influence of the rotor–rotor interactions is given in Fig. 27 for RPM 8000. For clarity, only wake elements from one blade are shown. The lower rotor (RHR) and its wake merge with the wake of the upper rotor (LHR) and directly interact with the LHR wake. Interactions cause variation of the blade loads and the variations increase with increasing RPM, as shown in Fig. 28, where the development of the normal force coefficient $C_N M^2$ is shown. The variations of $C_N M^2$ at two tip region sections and two RPM indicate that smooth variation of $C_N M^2$ values. The variation is slightly higher for RHR as it directly interacts with LHR wake. In general, the interaction is relative weak and smooth at these two sections.

5.1.3 Acoustics

Selected acoustic simulation results obtained at two microphone positions (M1($\Phi = 90^\circ, \theta = 0$), M2($\Phi = 90^\circ, \theta = -30^\circ$)) in the X–Z plane are compared with the test results, as shown in Figs. 29 and 30 for two rotor RPM. The spectral-averaged test data are chosen to better emphasize the relative importance of both the broadband and tonal components of the source.

For the microphone located at M1, the low-frequency BPF harmonics are the dominant source of noise and RHR

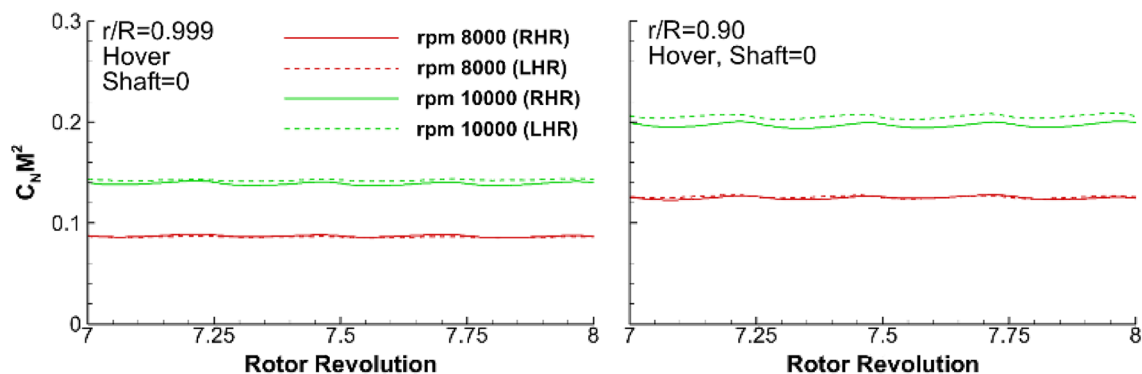


Fig. 28 Time history of $C_N M^2$ at two tip region sections for coaxial rotors in hover

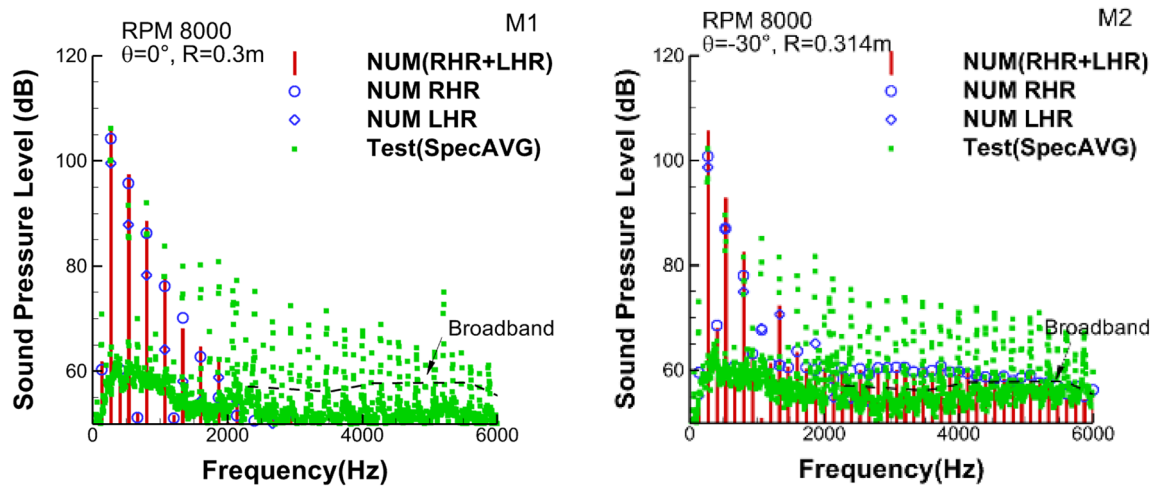


Fig. 29 Sound pressure level (SPL) spectra from microphones $\Phi=90^\circ$, $\theta=0^\circ, -30^\circ$ for RPM 8000

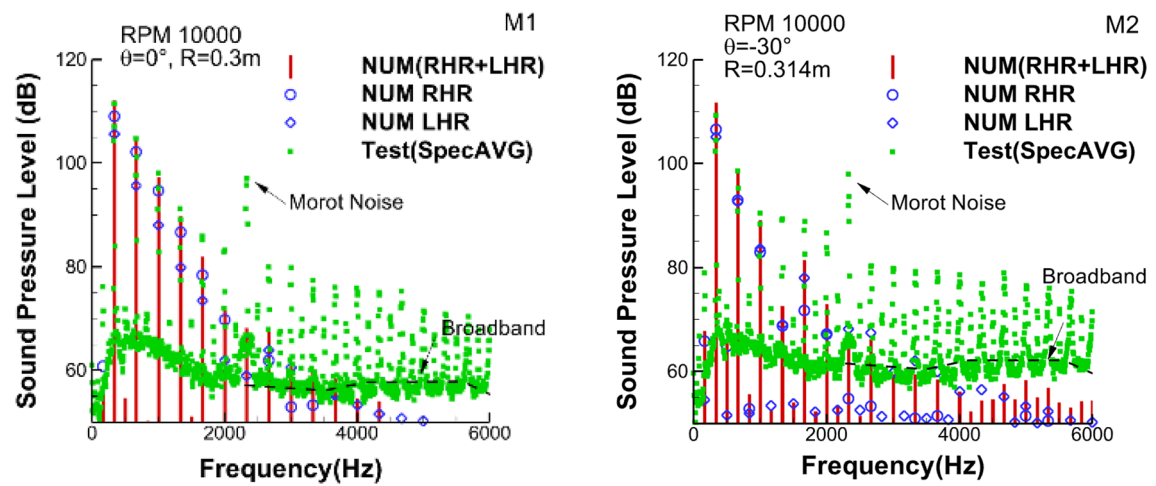


Fig. 30 Sound pressure level (SPL) spectra from microphones $\Phi=90^\circ$, $\theta=0^\circ, -30^\circ$ for RPM 10000

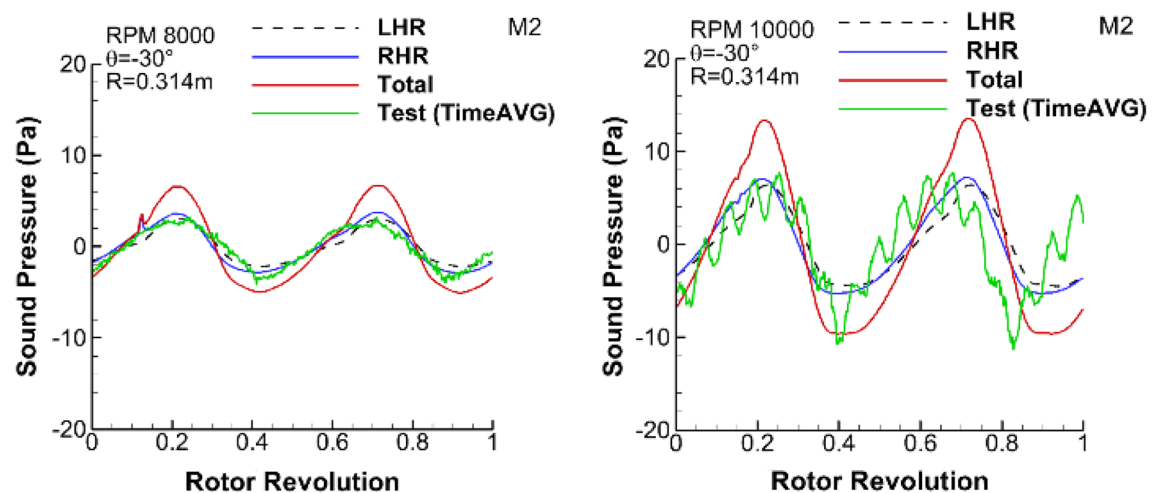


Fig. 31 Sound pressure time histories for the RHR, LHR, and a coherent sum of them

noise is dominant contributor to the SPL. In the test results, there is a clear increase in tonal component levels from the 3rd BPF harmonics upward for RPM 8000 and from the 5th BPF harmonics upward for RPM 10000. The increase in higher harmonic tonal component levels in the test may indicate more interactions related unsteadiness or an effect of the unsynchronized speed in the experiment.

For the microphone located at M2, both RHR and LHR noise are equally important contributors for first three tonal components and two RPM. Comparing with M1, the level dropdown for low-frequency harmonic value is much quicker, indicating less steady loading and thickness noise contribution to this microphone. An increase in higher harmonic tonal components is also observed. For lower harmonics, the difference between the simulation and the experiment is relative larger than that for the microphone at M1, especially for first BPF. This can be caused by the coherent summation used by the sum of two rotor components in the simulations. The effect of the coherent sum of the signal can be demonstrated more clearly in the time histories as shown in Fig. 31 for RPM 8000 and 10,000. For

a reference, a time-averaged test results are also included. Figure 31 shows clearly that the noises from the RHR and LHR are nearly identical and in-phase at this microphone position and the overall acoustic signal is almost doubled (solid red) in the peak region. Therefore, the coherent sum can increase OASPL in 6 dB. It should be mentioned that the coherent sum is necessary for rotors which are phase synchronized, and therefore, sum of the acoustic signal in time-domain is required. Due to slight asynchronization of RHR and LHR in the measurement, the time-averaging result (solid green) only matches the peak level from a single rotor. The high-frequency oscillations in the test result for RPM 10000 (Fig. 31 right) represent the contribution of the motor noise.

Acoustic assessments represented in overall sound pressure level (OASPL) on a 150 m hemisphere are shown in Figs. 32 and 33 for two RPM. The hemisphere is centered at the coordinate origin (Fig. 25) and underneath the rotors. For comparison, the noise from the isolated rotor as well as the noise from upper (LHR) and lower (RHR) rotor under interaction conditions are also given.

Fig. 32 Noise contours in OASPL on 150 m hemisphere underneath the rotors (RPM 8000)

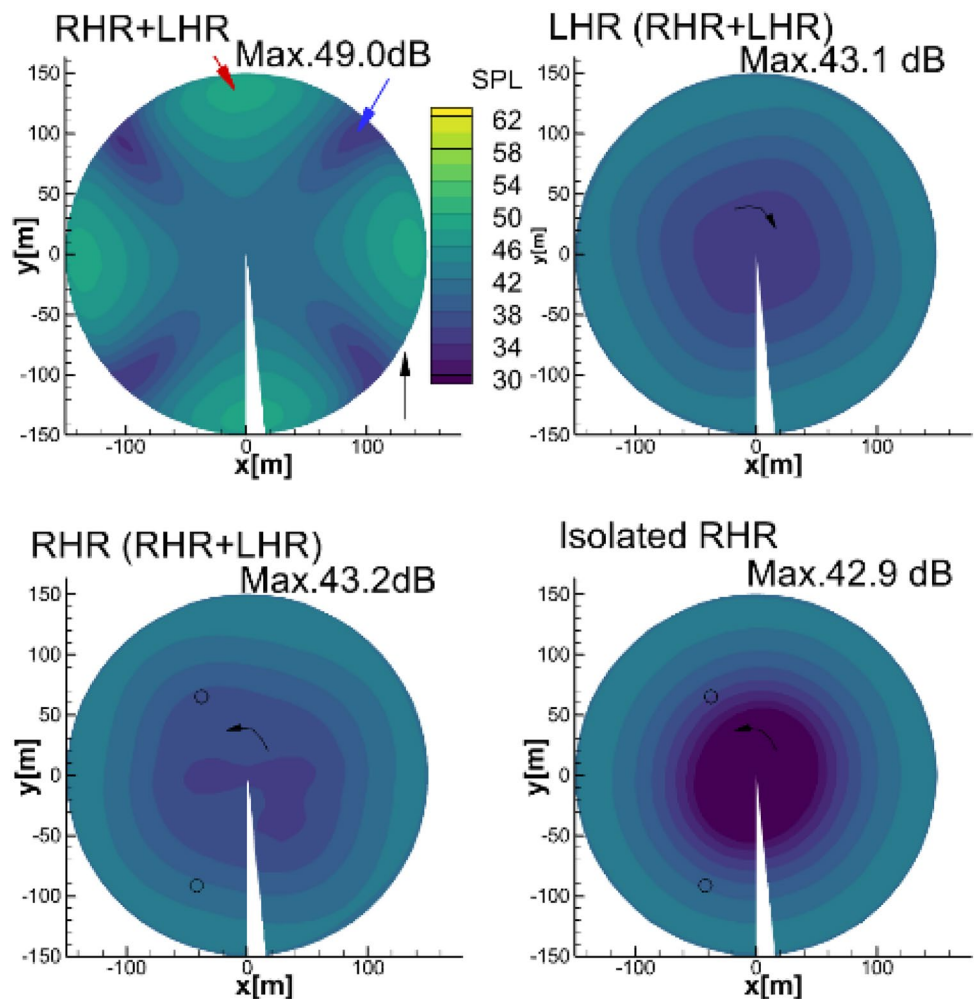


Fig. 33 Noise contours in OASPL on 150 m hemisphere underneath the rotors (RPM 10000)

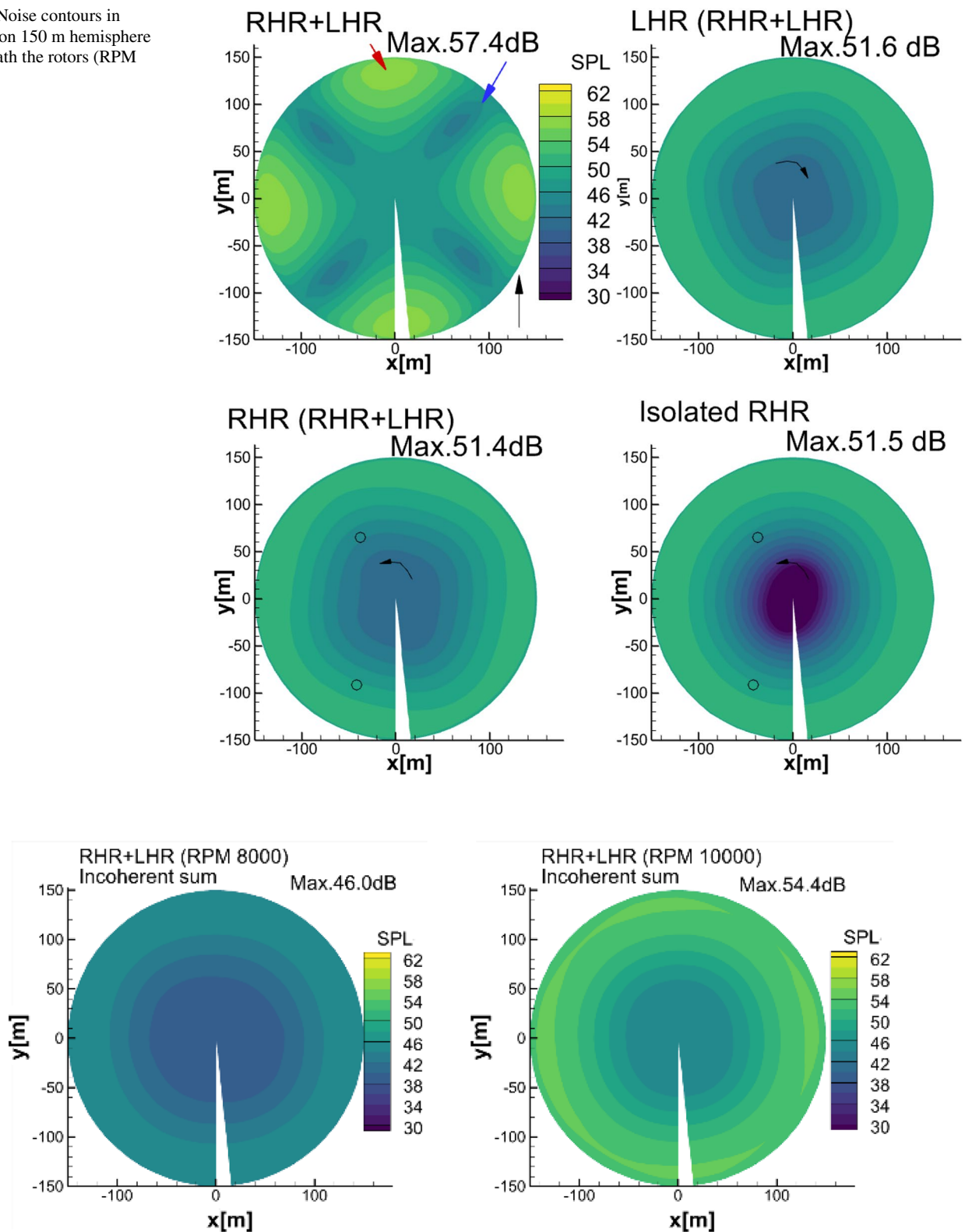


Fig. 34 Noise contours in OASPL on 150 m with an incoherent sum of RHR + LHR for RPM 8000, 10,000

The noise directivity for RHR (low left) and LHR (top right) in the coaxial condition for both RPM bears strong similarity to the isolated one (low right). The noise emission shows an increment of the noise level when the microphone moves away from the rotor axis, which demonstrates the typical characteristics of the contribution from the steady loading noise. The contour pattern is slightly deviated from the symmetric one. The noise level around the rotor axis increases in the coaxial condition, indicating the contribution from the unsteady loading noise.

Moreover, with the coherent sum (RHR + LHR) in time-domain, the interferences are particularly well visible in top left of Figs. 32 and 33. The contour pattern becomes more complex. The acoustic interference with acoustic signal cancelation (blue arrow) and enhancement (red arrow) is clearly seen.

In coaxial configuration, the maximum noise level for RHR and LHR deviated for both RPM from the isolated case by 0.1 and 0.3 dB, respectively. Compared to RHR or LHR, the maximum value for RHR + LHR increases about 5.8 and 5.9 dB, respectively, which corresponds to almost twice the sound pressure as indicated in Fig. 31.

It should be mentioned that the coherent sum is necessary for rotors which are phase synchronized. Therefore, the sum of the acoustic signal in time-domain is required. To show the influence of the acoustic interference using the coherent sum, the noise footprint with an incoherent sum of RHR + LHR is given in Fig. 34 for two RPM. It is observed that in the incoherent sum, the contour pattern deviates not significantly from RHR or LHR, as two rotors have similar noise directivity and no phase information from the acoustic signal is considered. Compared to the coherent sum, the maximum noise level is about 3 dB lesser than that of the coherent sum. For this hover configuration, the rotors

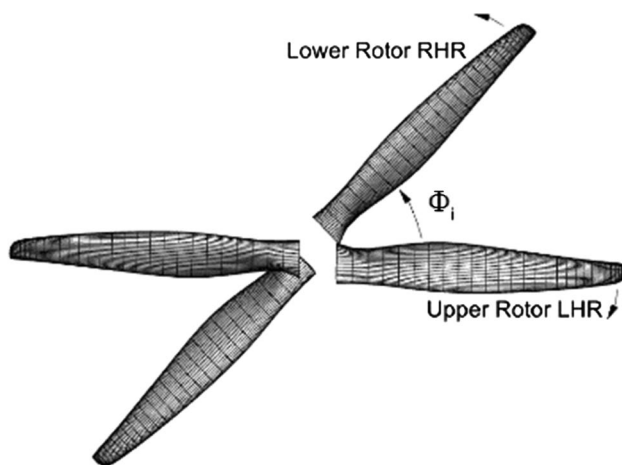


Fig. 35 Coaxial rotors with different starting phase delay (top view)

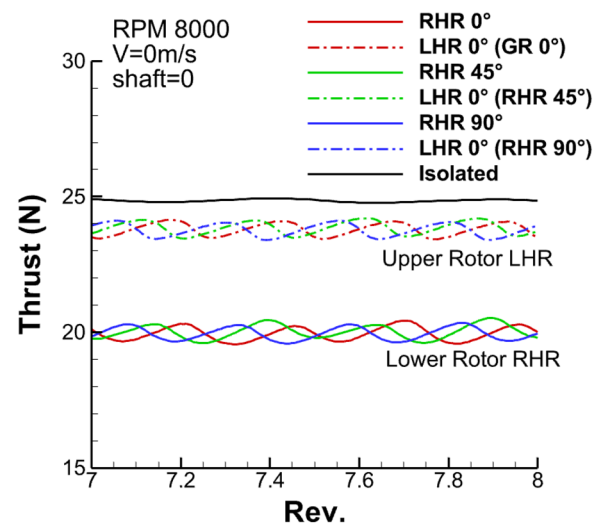


Fig. 36 Rotor thrust as a function of rotor revolution for different phase delay

operating at an incoherent condition is better for less maximum noise level.

In a real situation, the coherent level between the two rotors can be weaker than that for the full coherent case demonstrated here, because the asynchronization of the rotors, the noise scattering, or reflection from other components may change the phase information of the signal.

5.2 Hover at $\Delta z/D = 0.25$ for two rotors with two starting phase positions ($\Phi_i = 45^\circ$ and 90°)

In the previous section, the coherent sum shows strong acoustic interference effects. Therefore, two rotors with different starting phase position are simulated to show the effect of the phase delay between the rotors on the aerodynamic interaction and the acoustic interference.

The phase delay between the rotors are set at the rotor starting phase positions $\Phi_i = 45^\circ$ and 90° , respectively, as shown in Fig. 35. The phase delay is only applied on the lower rotor RHR. The starting position of the upper rotor LHR is fixed at $\Phi_i = 0^\circ$.

5.2.1 Aerodynamics

The trim conditions derived from Table 4 corresponding to $\Phi_i = 0^\circ$ are applied. There is no change on the time-averaged rotor thrust, indicating that the time-averaged inflow is not changed. The effect of the phase delay shows that the influence of RHR phase angle mainly shifts the positions of interaction peaks due to change the relative positions among the blades, as shown in Fig. 36.

Fig. 37 Total noise contour from the coherent sum (RHR + LHR in the time-domain)

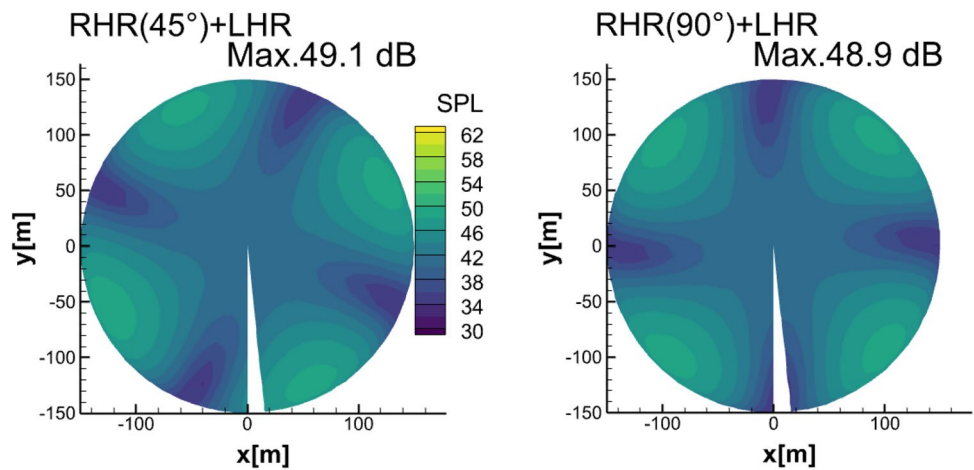


Table 5 Trim conditions

V_{∞} (m/s)	RPM	M_h	$\Delta\delta$ (deg)	T(N)	T(Test,N)
15	8000	0.41	RHR: - 1.46	22.7	22.7
			LHR: - 3.04	23.0	23.0
15	10,000	0.51	RHR: - 1.91	32.4	32.0
			LHR: - 2.51	37.0	37.0

5.2.2 Acoustics

Compared with the results without the phase delay as shown in the top left contour of Fig. 32, Fig. 37 shows the change on maximum sound pressure level only within 0.1 dB for both phase delays, except the rotation of the noise contour in an angle about the half of the phase delay. Therefore, the details of the potential fields, the interactions between the upper and lower rotor, as well as the details of the

wake-propeller interactions are not important for this configuration to define the maximum OASPL.

5.3 Forward flight at $\Delta z/D = 0.25$ for rotor starting phase positions at $\Phi = 0$

5.3.1 Trim conditions

The collective pitch correction to achieve test thrust is summarized in Table 5.

In forward flight, more pitch correction is required in comparison with the hover condition. Similar characteristics of two-per revolution force development like in the isolated case remain for the coaxial configuration, as shown in Fig. 38 for both RPM 8000 and RPM 10000. The multi-interaction causes the deviation of the two-per-revolution from a sinusoidal variation. For RPM 8000, there is only a very small difference in averaged thrust between RHR and LHR from the test. For RPM 10000, the thrust difference

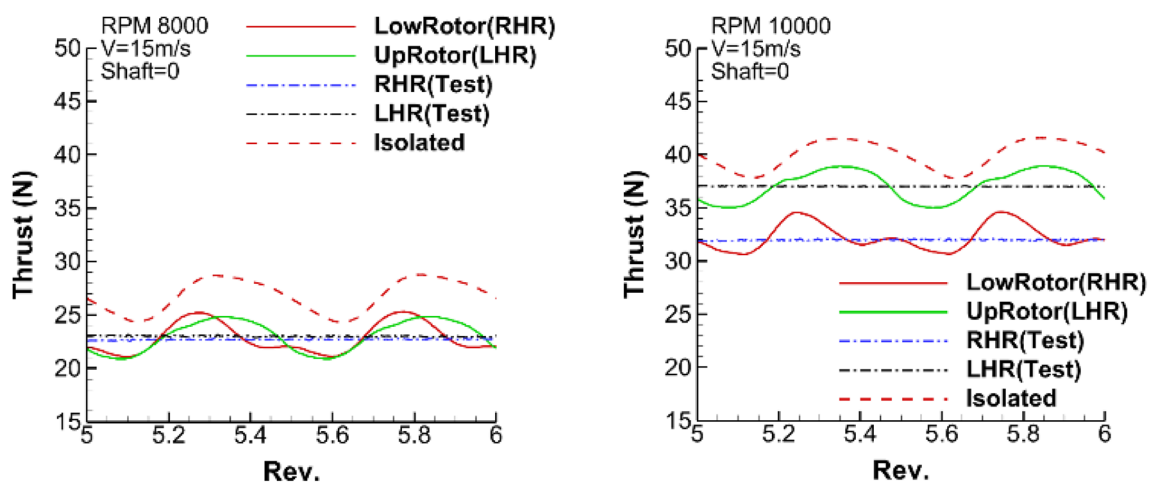


Fig. 38 Rotor thrust as a function of rotor revolution at RPM 8000 and 10,000

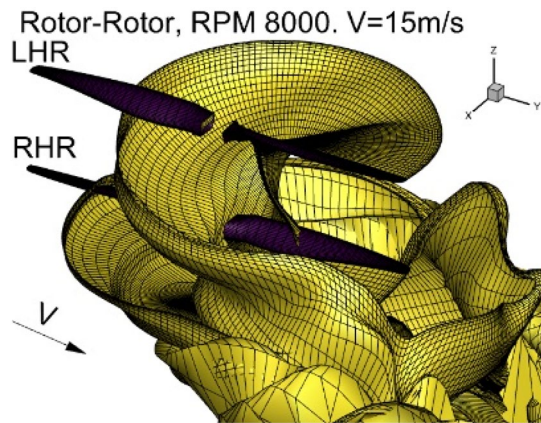


Fig. 39 Snap shot of coaxial-rotor wake development in forward flight

between the two rotors increases. The form of time histories is similar to that of RPM 8000.

5.3.2 Aerodynamics

A snap shot of the coaxial-rotor wake development in forward flight is given in Fig. 39 for RPM 8000. Similar to the hover condition, the merging of the LHR and the RHR wakes as well as direct interactions of the RHR with the LHR wake can be seen. Due to additional convection speed due to forward flight, the wakes move more quickly away from the rotor.

Figure 40 plots the development of the normal force coefficient $C_N M^2$. Compared to the isolated case in Fig. 22, the one per revolution (1-P) behavior due to the forward flight is also clearly seen, and in addition, multi-interactions of the wake and blades have caused many changes especially for the RHR in the first and fourth quadrant, where the loads

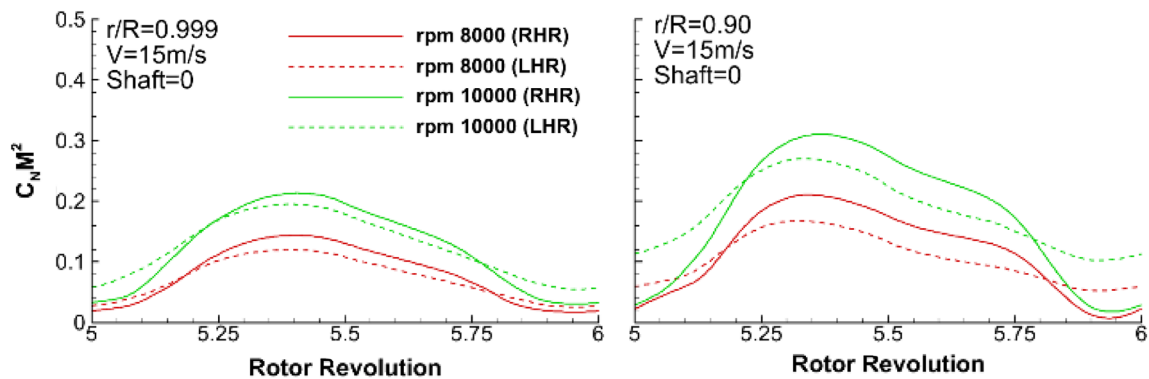


Fig. 40 Time history of $C_N M^2$ at two tip regions for coaxial rotor at forward flight

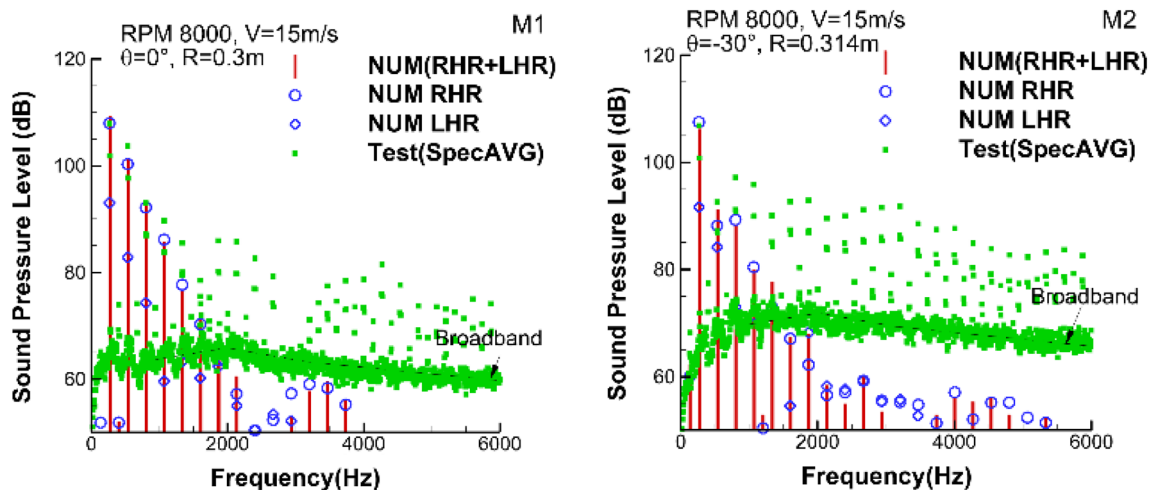


Fig. 41 SPL spectra at two microphone positions in the X-Z plane for RPM 8000

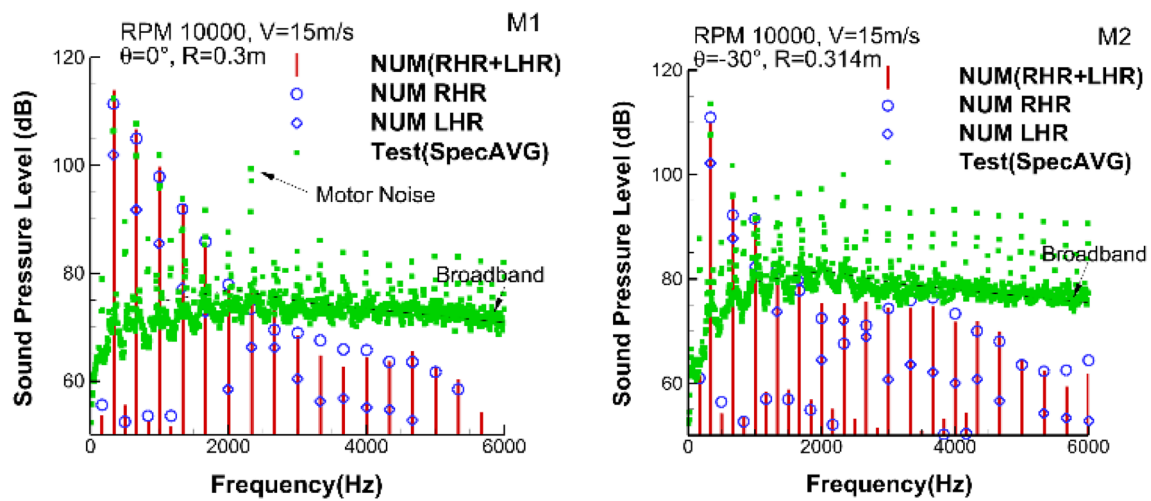


Fig. 42 SPL spectra at two microphone positions in the X-Z plane for RPM 10000

Fig. 43 Noise contours in OASPL on 150 m hemisphere underneath the rotors (RPM 8000)

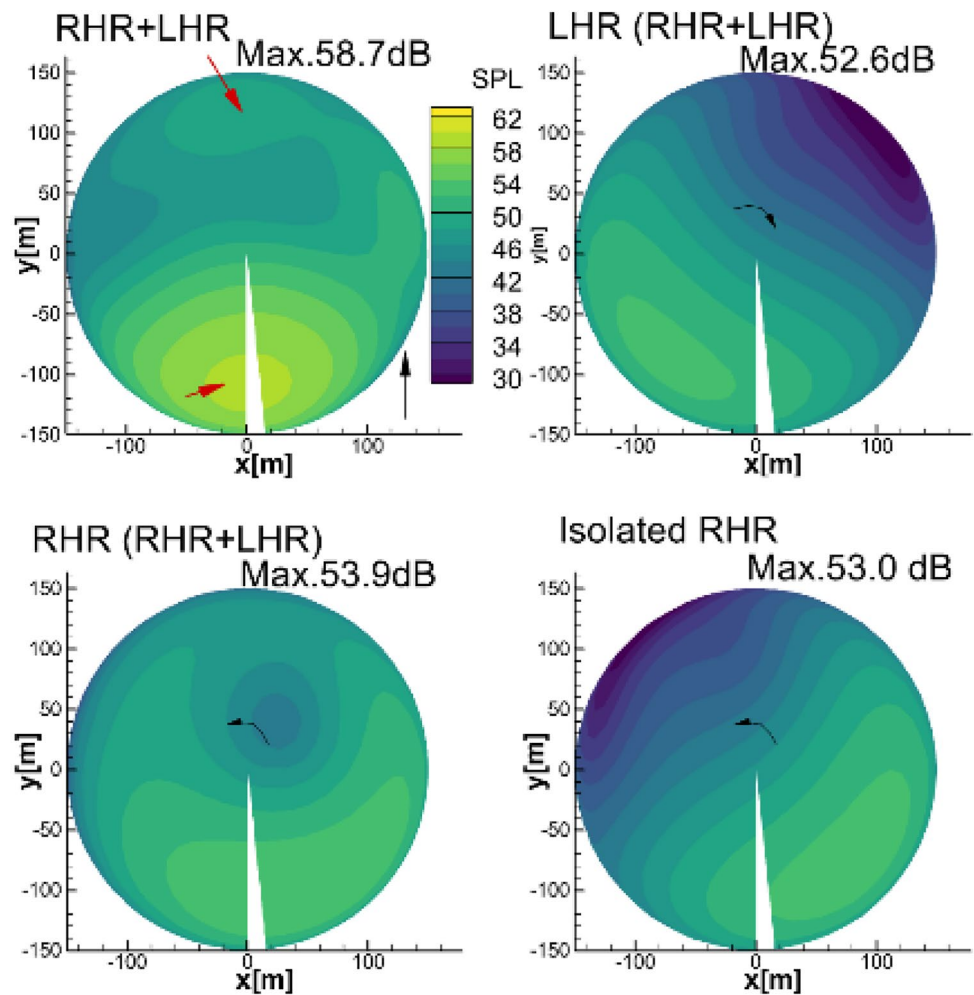
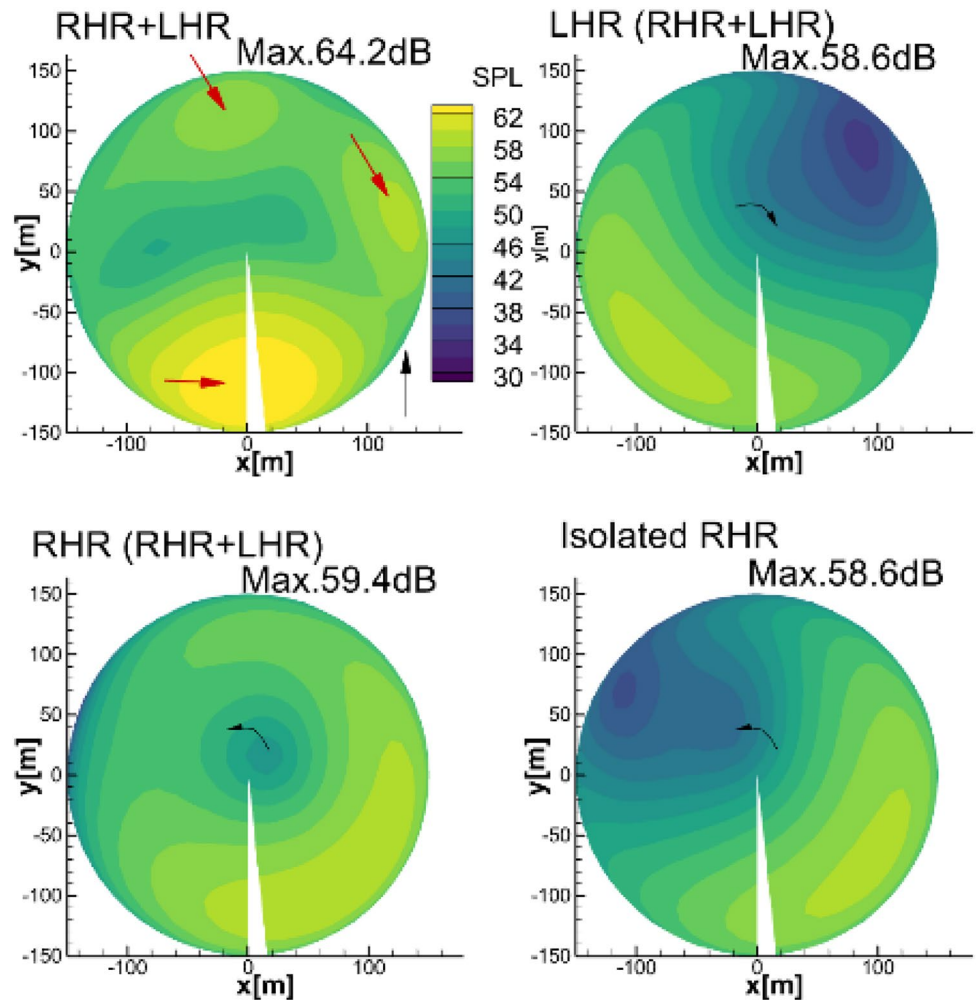


Fig. 44 Noise contours in OASPL on 150 m hemisphere underneath the rotors (RPM 10000)



difference between the two RPM are reduced. This indicates closer rotor–wake interactions.

5.3.3 Acoustics

The acoustic spectra obtained at two microphone positions [M1($\Phi = 90^\circ, \theta = 0^\circ$), M2($\Phi = 90^\circ, \theta = -30^\circ$)] are compared with the test results for RPM 8000 and 10,000 in Fig. 41 and Fig. 42. Both M1 and M2 are located in the X–Z plane, where M1 is also in the X–Y plane.

For the microphone M1, both numerical and experimental results show that the rotor harmonic noise till 3rd to 4th BPF from the RHR is the dominant source of noise for both RPM. The numerical and test results compare relative well in several low-frequency tonal components and deviate with each

other for the higher harmonics, indicating more unsteadiness in the test, which can be caused by leading-edge blade–wake interaction of the lower rotor.

For the microphone M2, numerical results in general underestimate the higher harmonics of the test results. Similar to M1, there is a clear increase in tonal component levels from the third BPF harmonics upward in the test. The broadband noise is significantly stronger compared with the M1 position. M2 is located in the plane below the rotational plane of the two rotors and may encounter the downwash flow from both rotors. Therefore, high broadband noise can partly also be attributed to the microphone self-noise.

It has to be mentioned that in the numerical simulation, the pylon wake is ignored and the influence of the pylon wake can be an additional reason for the differences.

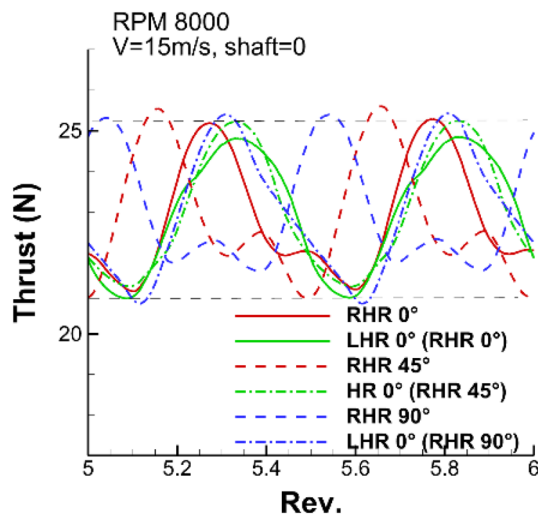


Fig. 45 Rotor thrust as function of rotor revolution for different phase delay

A comparison of the noise contour directivity for the overall sound pressure level is shown in Figs. 43 and 44 for RPM 8000 and 10,000, respectively. The noise directivity is characterized by the dominant loading noise for LHR, RHR, and RHR isolated. The acoustic interferences in RHR + LHR are well visible and shift the area of the maximum noise further downstream. The maximum noise level increases about 0.9 dB for the lower rotor (RHR) for both RPM, while 0.4 dB less noisy is observed for the LHR for RPM 8000. Compared to RHR or LHR, the coherent sum of both rotors increases the maximum noise level about 4.8 and 6.1 dB, respectively, which is similar to the analysis in the hover condition.

5.4 Forward flight at $\Delta z/D = 0.25$ for two rotors with two starting phase positions ($\Phi_i = 45^\circ$ and 90°)

Two rotors turning at RPM 8000 with different starting positions are simulated. The phase delay between the rotors are set at 45° and 90° , respectively. The phase delay is only applied on the lower rotor RHR, as shown in Fig. 35. The starting position of the upper rotor LHR is fixed at $\Phi_i = 0^\circ$ and points to the downstream.

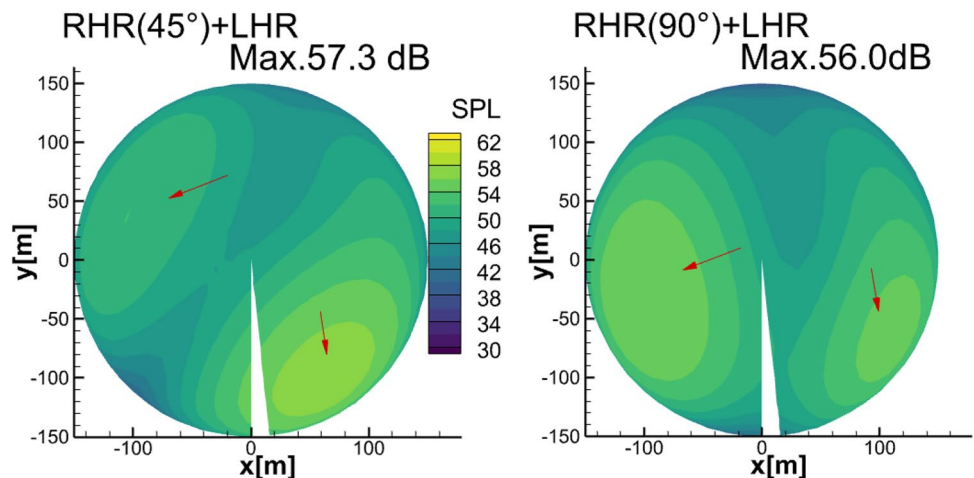
5.4.1 Aerodynamics

The trim conditions derived from Table 5 are applied. There is no additional correction on the blade pitch angel required. Therefore, the time-averaged inflow is not changed by the phase angles. Compared with the results without the phase delay as shown in Fig. 45 for RPM 8000 in solid line, the effect of the phase delay changes not only the positions of maximum peaks, but also changes both the form and the amplitude of the curve. There is a slight increase in the amplitude when applying the phase angle.

5.4.2 Acoustics

OASPL contours for the two-phase angles are given in Fig. 46 for RPM 8000. Compared with the results without the phase angle as shown in Fig. 43 top left, the change of both the noise directivity and the maximum noise level are observed. Due to the change of the signal phase angle introduced by the blade phase delay, the interference peaks pointed by red arrows are rotated count-clockwise. The maximum level reduces about 1.4 dB for 45° and 2.7 dB for 90° , respectively.

Fig. 46 OASPL contour from the coherent sum of the RHR + LHR for RPM 8000



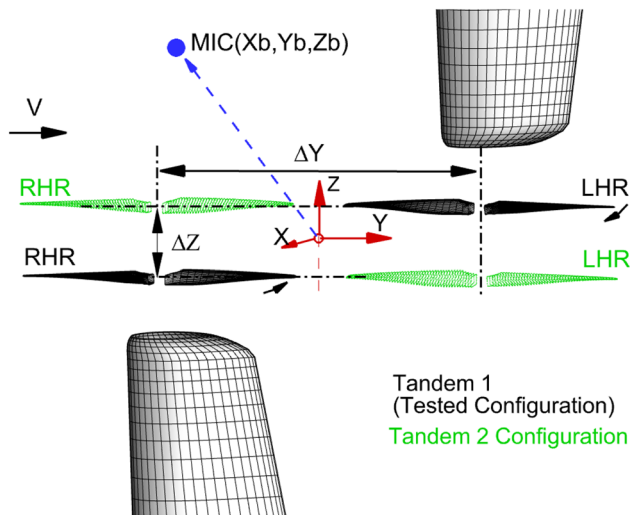


Fig. 47 Coordinate and geometric definition for the tandem rotor configurations

6 Results for two rotors in two tandem conditions

For the tandem configuration, both rotors are in a plane which is parallel to the y - x plane. The origin of the coordinate system lies at the mid-point between both rotor axes. Both rotors turn in opposite direction with the same rotational speed. The upstream rotor defined as right-handed

Table 6 Trim conditions ($V_\infty = 15$ m/s)

Tandem	RPM	M_h	$\Delta\delta$ (deg)	T(N)	T(Test, N)
1	8000	0.41	RHR: -2.51	26.4	26.3
			LHR: 0.83	24.7	25.0
2	8000	0.41	RHR: -2.42	26.3	26.3
			LHR: -1.53	24.5	25.0

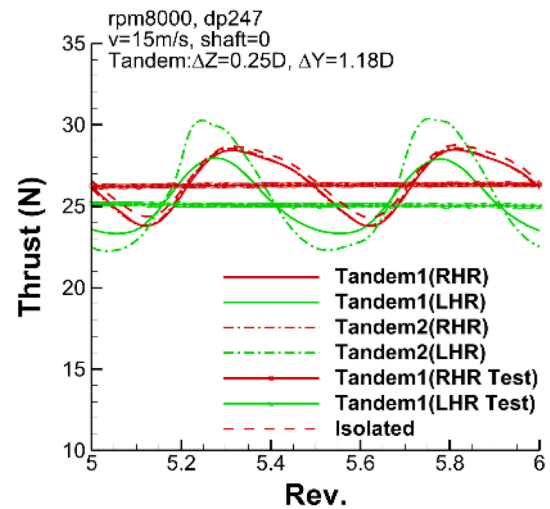


Fig. 49 Rotor thrust as function of rotor revolutions in two tandem configurations

rotor (RHR) rotates count-clockwise and the downstream rotor defined as left-handed rotor (LHR) rotates clockwise. Results for the tandem configurations with $\Delta Y = 1.18D$ and $\Delta Z = \pm 0.25D$ are studied:

1. Tandem 1: the downstream rotor located above the upstream rotor, $\Delta Z = 0.25D$, as shown in black in Fig. 47.
2. Tandem 2: the downstream rotor located below the upstream rotor, $\Delta Z = 0.25D$, as shown in green in Fig. 47. As no test conducted, the thrust from tandem 1 is used.

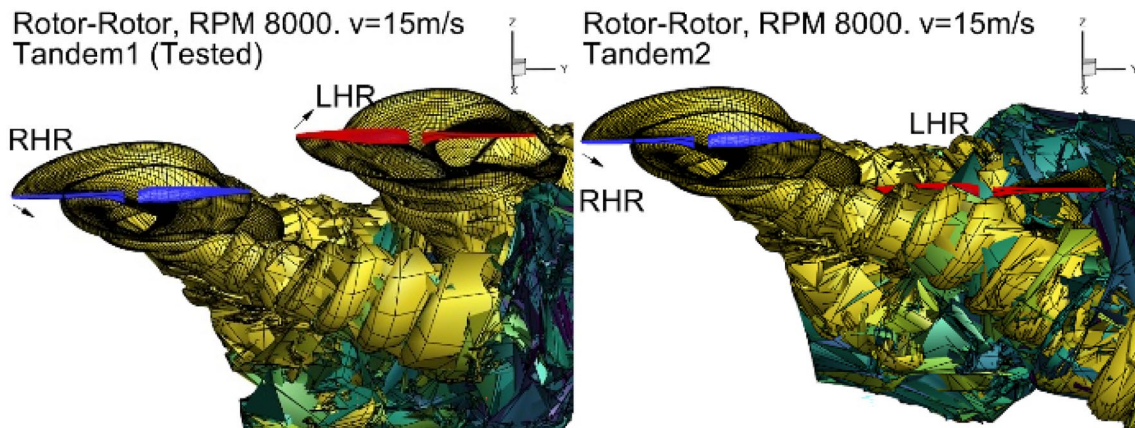


Fig. 48 Snap shot of the rotor wake development in the tandem configurations; top: tandem 1 and bottom: tandem 2

6.1 Forward flight for two rotors with same starting position

6.1.1 Trim conditions

The collective pitch correction to achieve test thrust is summarized in Table 6.

The multi-interaction causes a deviation of the two-per-revolution form noticed for the isolated case. The form of the LHR thrust in one rotor revolution deviates strongly from the form of the RHR. This indicates that the influence of the RHR/LHR multi-induction has a much stronger effect on the LHR, especially for the tandem 2 configurations. The thrust form of the upstream rotor (RHR) is less affected by the interactions, which has very similar form and amplitude like isolated one.

6.1.2 Aerodynamics

Two snap shots of the rotor wake development for the two tandem configurations are shown in Fig. 48. For the tandem 1 configuration, the wakes from upstream rotor (RHR) convect down stream and pass underneath the downstream rotor (LHR). In the far field, both rotor wakes merge. For the tandem 2 configuration, the RHR wakes pass very close to and partly through the LHR and its wakes. The rolled-up wing tip like wakes of the RHR hit the LHR and deform the LHR wake strongly. The strong induction of the RHR wake distorts and absorbs the LHR wake. The direct interactions of the RHR wakes can cause strong variation in the rotor aerodynamic, as shown in Fig. 49.

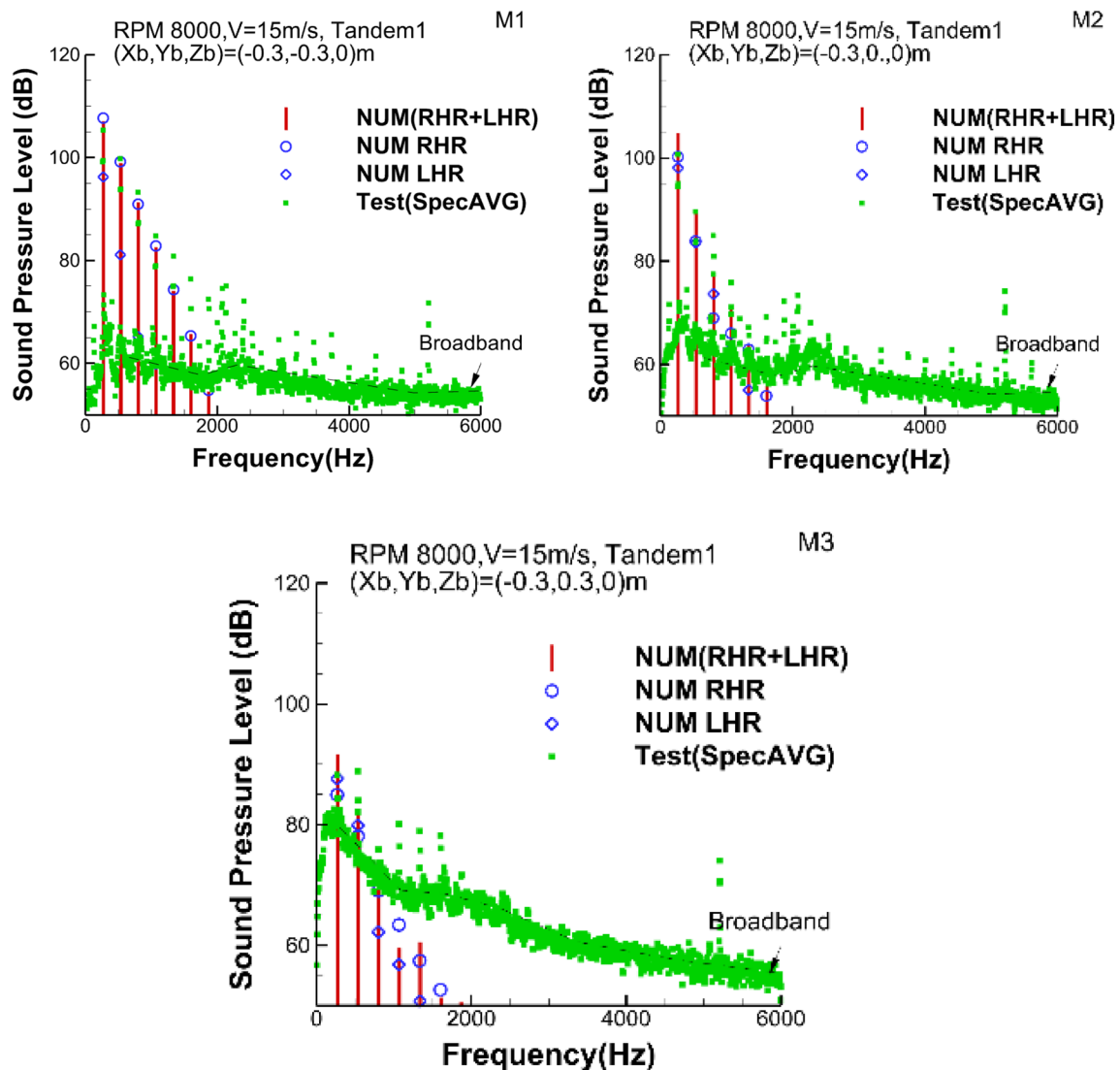


Fig. 50 SPL spectra from the microphone located at M1 to M3

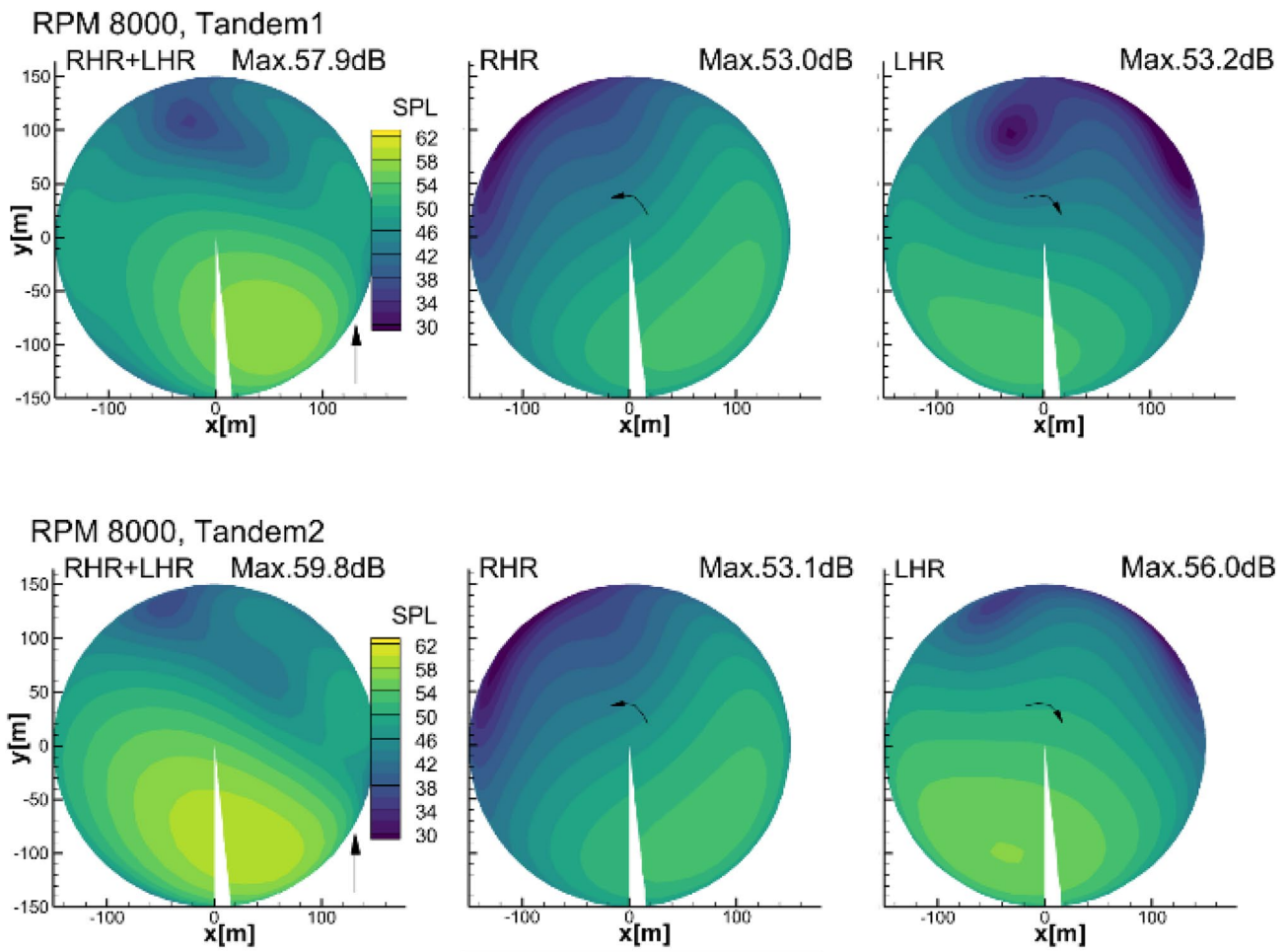


Fig. 51 Noise contours directivity on 150 m hemisphere for two tandem configurations

6.1.3 Acoustics

The acoustic spectrums obtained at three microphone positions in the X–Y plane for the Tandem 1 configuration are compared with the test results in Fig. 50. Three microphones are located at the upstream of RHR (M1), and up (M2)- and downstream (M3) of LHR, respectively.

For M1, the first four low-frequency BPF harmonics are the dominant source of noise. For these four BPFs, the RHR noise is the dominant contributor to the noise level. At first BPF, the contribution of the LHR reduces slightly the overall noise. This indicates that the acoustic signal from the RHR and the LHR is slightly out of phase and some cancelation of two signal occurs for this microphone. In the test results, there is a clear increase in tonal component levels from the 5th BPF harmonics upward, but their contributions to the OASPL can be neglected.

For M2, the noise from both the RHR and the LHR is equally important for first two BPFs. Therefore, the influence of the acoustic interference effect between the rotors

can be stronger than M1. The summation of the RHR and the LHR enhances the noise level till 3rd BPF. This indicates that the acoustic signal from the RHR and the LHR is in-phase. Compared with M1, the level dropdown with increasing the frequency is much quick, indicating less steady loading noise contribution.

For M3, there is increasing broadband noise or background flow noise in the test, as the M3 is located at the downstream of the two rotors. At this position, the microphone may already be located in the induced flow area where the axis of the microphone may largely deviate from the flow stream line. This increases the background noise due to the flow interaction with the inflow microphone.

A comparison of the noise contour directivity for the two tandem configurations is shown in Fig. 51. The noise directivity for both configurations bears strong similarity. The noise emission shows an increment of the noise level for tandem 2 due to higher the interaction noise for the downstream rotor. The maximum noise level for tandem 2 increases about 2 dB.

7 Concluding remarks

The acoustic and aerodynamic characteristics of small multirotor configurations for various flight conditions are simulated and compared with available test data. An unsteady free wake panel code was used to account for the influence of the rotor–rotor interactions. The acoustic characteristics were calculated with an FW–H code. To evaluate the rotor noise shielding effects by the support pylon, a Fast Multipole Boundary-Element Method (BEM) which solves the exterior Helmholtz problem for the scattered pressure field is used.

For isolated rotor cases, rotor tone components in the form of harmonics of the rotor blade passage frequency are the dominant source of the rotor noise, but they are dominant only for the first few harmonics as blade tip Mach numbers are relatively low. Broadband noise is observed in the test, but the contribution to the overall sound pressure is small. The acoustic scattering from the rotor support system for the isolated rotor cases indicated an influence about 1 to 3 dB on the overall sound pressure, depending on the positions of the microphones. In forward flight, the decay rate of the tone noise is relatively slow, as increasing the unsteady noise. There is increasing broadband noise or background flow noise in the test, but still remaining well below the rotor contribution. In general, it is preferable to use rotor with possible low RPM to reduce the noise radiation.

For rotor/rotor cases, the multi-inductions of wake downwash, rotor potential, and displacement field cause deformations of the wakes and reduce the effective angle of attack of both rotors, especially lower rotor, and therefore reduce the rotor thrust in comparing with isolated rotor cases. The rotor tone components are still a dominant source and the results indicated that the noise emission of the rotors can be affected by multi-interactions. In the coaxial configuration, the acoustic interferences are particularly well visible in the numerical simulation. The interference can increase or decrease the maximum noise level. In general, the rotors operating at an incoherent condition are better for less maximum noise level. The study of the phase delay between the rotors indicated that in the forward flight, the phase delay can be used to reduce the noise radiation. The study of the tandem configuration showed that the position of the downstream rotor is key for the noise radiation, and therefore, avoiding the interaction with upstream wake can reduce the noise radiation.

The motor noise contributes to all the rotor harmonics and its subharmonics, but the motor noise overwhelms the rotor contributions only at specific harmonics.

Acknowledgements The research leading to the presented results has been addressed within the framework of both DLR AACID (Acoustics and aerodynamics for city drones) project and the HC/AG-26 Noise Radiation and Propagation for Multirotor System Configurations, supported by GARTEUR.

Funding Open Access funding enabled and organized by Projekt DEAL.

Data availability Not applicable.

Declarations

Conflict of interest The authors declare that they have no conflict of interest.

Open Access This article is licensed under a Creative Commons Attribution 4.0 International License, which permits use, sharing, adaptation, distribution and reproduction in any medium or format, as long as you give appropriate credit to the original author(s) and the source, provide a link to the Creative Commons licence, and indicate if changes were made. The images or other third party material in this article are included in the article's Creative Commons licence, unless indicated otherwise in a credit line to the material. If material is not included in the article's Creative Commons licence and your intended use is not permitted by statutory regulation or exceeds the permitted use, you will need to obtain permission directly from the copyright holder. To view a copy of this licence, visit <http://creativecommons.org/licenses/by/4.0/>.

References

1. Straubinger, R. Rothfeld, M. Shamiyeh, K.-D. Büchter, J. Kaiser and K. O. Plötner, “An overview of current research and developments in urban air mobility—Setting the scene for UAM introduction”, *Journal of Air Transport Management*, Bd. 87, Nr. , p. 101852, 2020.
2. Johnson, W., Silva, C.: NASA concept vehicles and the engineering of advanced air mobility aircraft. *The Aeronautical Journal* **126**(1295), 59–91 (2022)
3. W. Johnson and C. Silva, “Concept vehicles for VTOL air taxi operations”, AHS Technical Conference on Aeromechanics Design for Transformative Vertical Flight, American Helicopter Society (AHS), 2018.
4. H. Kim, A. Perry and P. Ansell, “A Review of Distributed Electric Propulsion Concepts for Air Vehicle Technology”, AIAA/IEEE Electric Aircraft Technologies Symposium, AIAA Paper 2018–4998, 2018, <https://doi.org/10.2514/6.2018-4998>.
5. Tinney and J. Valdez, “Thrust and Acoustic Performance of Small-Scale, Coaxial, Corotating Rotors in Hover”, *AIAA JOURNAL* Vol. 58, No. 4, April 2020, <https://doi.org/10.2514/1.J058489>
6. N. Zawodny and D. Douglas Boyd, Jr., “Investigation of Rotor–Airframe Interaction Noise Associated with Small-Scale Rotary-Wing Unmanned Aircraft Systems”, *Journal of the American Helicopter Society*, Volume 65, Number 1, January 2020, pp. 1–17(17), <https://doi.org/10.4050/JAHS.65.012007>
7. N. Zawodny, A. Christian and A. Cabell, “A Summary of NASA Research Exploring the Acoustics of Small Unmanned Aerial Systems”, AHS International Technical Conference on Aeromechanics Design for Transformative Vertical Flight, Paper 46, San Francisco, CA, January 16–18, 2018.
8. Theodore, “A Summary of the NASA Design Environment for Novel Vertical Lift Vehicles (DELIVER) Project”, AHS International Technical Conference on Aeromechanics Design for Transformative Vertical Flight, Paper 64, San Francisco, CA, January 16–18, 2018.
9. Tinney and J. Sirohi, “Multirotor Drone Noise at Static Thrust”, *AIAA JOURNAL* Vol. 56, No. 7, July 2018, <https://doi.org/10.2514/1.J056827>

10. M. Pott-Pollenske, J. W. Delfs, "Enhanced Capabilities of the Aeroacoustic Wind Tunnel Braunschweig", 14th AIAA/CEAS Aeroacoustics Conference (29th AIAA Aeroacoustics Conference), 2008, AIAA-2008-2910.
11. K.-S. Rossignol, J. Yin und L. Rottmann, "Investigation of Small-Scale Rotor Aeroacoustic in DLR's Acoustic Wind Tunnel Braunschweig", in 28th AIAA/CEAS Aeroacoustics 2022 Conference., Southampton, UK, 2022.
12. J. Yin "Prediction - and its Validation - of the Acoustics of Multi-blade Rotors in Forward Flight Utilising Pressure Data from a 3-D Free Wake Unsteady Panel Method". Proceedings, 20th European Rotorcraft Forum, 04.—07.10.1994 in Amsterdam/Niederlande.
13. S.R. Ahmed, V.T. Vidjaja, "Unsteady Panel Method Calculation of Pressure Distribution on BO105 Model Rotor Blades", Journal of the American Helicopter Society, pp. 47–56, Jan. 1998.
14. J. Yin, S.R. Ahmed, "Helicopter main-rotor/tail-rotor interaction". Journal of the American Helicopter Society, Vol. 45 (No. 4), pp. 293 -302, 2000.
15. J. Yin, B.G. van der Wall, G.A. Wilke "Rotor Aerodynamic and Noise under Influence of Elastic Blade Motion and Different Fuselage Modeling". 40th European Rotorcraft Forum (ERF) 2014, 2–5 September 2014, Southampton, UK.
16. P. Kunze, "Approximate Boundary Layer Methods for a Fast Mid-Fidelity Aerodynamics Code for Helicopter Simulations". Springer Nature Switzerland. New Results in Numerical and Experimental Fluid Mechanics XIII, Virtuell. https://doi.org/10.1007/978-3-030-79561-0_36. ISBN 978-3-030-79560-3. ISSN 1612-2909, 2021
17. M. Tugnoli, D. Montagnani, M. Syal, G. Droandi A. Zanotti, "Mid-fidelity approach to aerodynamic simulations of unconventional VTOL aircraft configurations". Aerospace Science and Technology 115, 2021
18. Schwarmborn, T. Gerhold, R. Heinrich, "The DLR TAU-Code: Recent Applications in Research and Industry", Proceedings of European Conference on Computational Fluid Dynamics ECCO-MAS CFD 2006, Delft, Netherlands.
19. M. Lummer, C. Richter, C. Proeber, J. Delfs, "Validation of a model for open rotor noise predictions and calculation of shielding effects using a fast BEM," 19th AIAA/CEAS Aeroacoustics Conference, Berlin, Germany, 27.-29. Mai 2013. <https://doi.org/10.2514/6.2013-2096>
20. J. Yin, "Investigation of Rotor Noise Shielding Effects by the Helicopter Fuselage in Forward Flight". Journal of Aircraft, 56 (4), Seiten 1–12. American Institute of Aeronautics and Astronautics (AIAA). <https://doi.org/10.2514/1.C035009>. ISSN 0021-8669.
21. S. Balay, S. Abhyankar, M. F. Adams, J. Brown, P. Brune, K. Buschelman, L. Dalcin, V. Eijkhout, W. D. Gropp, D. Kaushik, M. G. Knepley, L. C. McInnes, K. Rupp, B. F. Smith, S. Zampini, H. Zhang, "PETSc Users Manual", Tech. Rep. ANL-95/11 - Revision 3.7, Argonne National Laboratory, 2016.

Publisher's Note Springer Nature remains neutral with regard to jurisdictional claims in published maps and institutional affiliations.